



Two-Dimensional Hybrid Halide Perovskites: Synthesis, Properties, and Applications

Joseph Wong^{1,2}, Kesong Yang^{1,3,4,*}

¹Department of NanoEngineering and Program of Chemical Engineering, University of California San Diego, La Jolla, California 92093-0448, USA

²Boeing Commercial Airlines, 3003 Casino Rd, Everett, WA 98204

³Program of Materials Science and Engineering, University of California San Diego, La Jolla, California 92093-0418, USA

⁴Center for Memory and Recording Research, University of California San Diego, La Jolla, California 92093-0401, USA

The hybrid organic–inorganic halide perovskites have experienced a surge of attention in the past decade because of their promising applications in the next-generation solar cells, with a remarkable improvement of the power conversion efficiency (PCE) from 3.8% to 25.2%. As the next-generation hybrid halide perovskites, two-dimensional hybrid perovskites (2DHPs) expand the connotation of hybrid materials and demonstrate potential to offer higher tunability and more excellent materials properties than the three-dimensional hybrid perovskites as a result of the reduced dimensionality. In this article, we present a review on the current research progress of the 2DHPs, including structural characterization, materials synthesis approaches, optoelectronic and multiferroic properties, defect states, moisture stability, and related devices and applications, along with their related computational and theoretical studies. We conclude the review with a discussion of the current challenges and future directions in the field.

I. Introduction

The hybrid organic-inorganic halide perovskites have emerged as one class of most promising light-harvesting materials for the next-generation solar cells because of their exceptional optoelectronic properties and low-temperature solution processability that allow for large-scale fabrication.[1–14] The hybrid halide perovskites are one class of semiconductors in a formula of ABX_3 that comprises a network of corner-sharing BX_6 octahedra. In this structure, A is an organic cation such as methylammonium (MA: $CH_3NH_3^+$); B is a divalent metal cation such as Pb^{2+} and Sn^{2+} , located in the center; and X is a monovalent anion such as Cl^- , Br^- , and I^- . These structural and compositional features determine their exceptional optoelectronic properties such as tunable bandgaps,[6–11] high absorption coefficient,[7–9,12–14] long carrier diffusion length[14–17] and lifetime,[6, 17–23] low trap density,[16, 17] and high carrier mobility.[7, 8,14,17, 24–27] Just in the past few years, the power conversion efficiency (PCE) of these halide perovskites solar cells at lab-scale testing has increased from 3.8% to 25.2% (in the perovskite/silicon tandem device).[28]

Despite promising applications of halide perovskites in the photovoltaic industry, there are still several major challenges that inhibit their large-scale industrial applications.[29–32] These challenges include poor stability in ambient conditions, particularly in the moisture environment,

This article has been accepted for publication and undergone full peer review but has not been through the copyediting, typesetting, pagination and proofreading process, which may lead to differences between this version and the [Version of Record](#). Please cite this article as doi: [10.1002/solr.202000395](https://doi.org/10.1002/solr.202000395)

This article is protected by copyright. All rights reserved

and the demand for lead-free perovskites. For instance, $(\text{MA})\text{PbI}_3$ will degrade into MAI and PbI_2 in ambient conditions in which the water molecules will facilitate the degradation process, sharply dropping perovskite thin film absorption in a matter of days.[33] Although encapsulation can mitigate the degradation from water molecules,[34] the hybrid perovskites were considered as intrinsically unstable in the long term due to unfavorable formation enthalpies.[35, 36]

Two-dimensional hybrid perovskites (2DHPs) offer a promising solution to overcome this instability issue.[37–47] The two-dimensional nature refers to the layer structure of corner-sharing inorganic octahedra. These inorganic metal halide layers are interdigitated between bulky organic molecules such as butylammonium (BA: $\text{C}_4\text{H}_9\text{NH}_3^+$). The bulky organic molecules are bonded to the inorganic octahedra via hydrogen bonds, causing the large hydrophobic chain to orient away from the inorganic perovskite layers. This configuration forms organic bilayers that separate neighboring sheets, creating a repeating pattern of organic and inorganic layers that define the 2DHP crystal structure, see Figure 1.

Fig. 1: Schematic representation of the three types of 2DHPs. (a) RP-type perovskite phase, $\text{Ca}_4\text{Mn}_3\text{O}_{10}$ and $(\text{BA})_2(\text{MA})_2\text{Pb}_3\text{I}_{10}$; (b) DJ-type perovskite phase, $\text{CsBa}_2\text{Ta}_3\text{O}_{10}$ and $(3\text{AMP})(\text{MA})_2\text{Pb}_3\text{I}_{10}$; (c) ACI-type perovskite phase, $(\text{GA})(\text{MA})_n\text{Pb}_n\text{I}_{3n+1}$ ($n = 1-3$).
Reproduced and adapted from Refs. [48] and [49].

2DHPs demonstrate some advantageous materials properties compared to the three-dimensional (3D) hybrid perovskites (3DHPs), including high materials stability and robustness in the presence of water,[39, 50] reasonable performance, and cheap solution processability.[37, 51–54] Moreover, the interchangeability of the large organic cations and the control of layer dimensionality allow for greater tunability and flexibility of the physical and optoelectronic properties.[47, 53–56] Compared to 3DHPs, 2DHPs show more expandable optoelectronic properties such as larger exciton binding energies, enabling enhanced photoluminescence (PL) properties for room-temperature light-emitting-diode (LED) applications.[51, 57, 58]

In this review article, we provide an overview of current research progress of the 2D hybrid halide perovskites, including their structural features, synthesis approaches, materials properties, and applications. In particular, the fundamental aspects of the 2DHPs including the optoelectronic and defect properties, and materials stability are highlighted along with related computational and theoretical studies from first-principles density functional theory (DFT) calculations. The challenges and future research directions of this class of materials are discussed.

II. Structures

2DHPs have been found with three types of phase structures, including Ruddlesden-Popper (RP) phase, Dion-Jacobson (DJ) phase, and so-called ACI phase, as shown in Figure 1. The RP phase has a general form $\text{R}_2(\text{MA})_{n-1}\text{M}_n\text{X}_{3n+1}$, where R is an aliphatic or aromatic alkylammonium cation, MA is methylammonium ($\text{C}_2\text{H}_5\text{NH}_3^+$), M is a metal cation with a 2+ oxidation state (such as Pb, Sn, and Ge), X is a halide anion (such as I, Br, and Cl), and n is the dimensionality. In the RP phase perovskites, the inorganic layers are offset by one octahedral unit with an in-plane displacement, see Figure 1a. The DJ phase has a formula $\text{R}'(\text{MA})_{n-1}\text{M}_n\text{X}_{3n+1}$, in

which the large organic cation R' has a 2+ charge leading to only one organic cation between each inorganic layer.[48] In the DJ phase perovskites, the divalent organic cations connect two adjacent inorganic layers by forming hydrogen bonds on both ends, and thus the adjacent inorganic layers can be stacked on top of each other without offsets, see Figure 1b. The ACI phase has a formula $R(\text{MA})_n \text{M}_n \text{X}_{3n+1}$, in which the small MA cations fill both in the inorganic sheets and in the interlayer with the large R cations, adopting the structural features of both RP and DJ phases and thus a higher crystal symmetry than the RP phase.[49], see Figure 1c.

The dimensionality, n , indicates the number of inorganic sheets placed between each organic layer. At $n = 1$, the formula can be simplified as $(\text{R})_2 \text{MX}_4$, a strict 2D material such as $(\text{BA})_2 \text{PbBr}_4$. [59] At $n \geq 2$, the formula includes the MA cation, describing a quasi-2D perovskite material where the MA cation is intercalated between inorganic layers such as in $(\text{PEA})_2 (\text{MA})_2 \text{Pb}_3 \text{Br}_{10}$. [54] At $n = \infty$, the formula can be rewritten as $(\text{MA})\text{MX}_3$, a 3D perovskite such as $(\text{MA})\text{PbI}_3$. [9] An illustration of the structural evolution for the 2DHP, $(\text{BA})(\text{MA})_n \text{Ge}_n \text{I}_{3n+1}$, as a function of n ($n = 1-3$) is shown in Figure 2a. The experimental characterization of geometrical structures is often carried out from X-ray diffraction (XRD), [37, 59–61] as shown in Figure 2b-c.

The 2DHP is composed of inorganic layers of $[\text{MX}_6]^{4-}$ interdigitated with organic cation bilayers. Several guidelines have been proposed for selecting suitable organic cations for incorporation within the layered perovskite frameworks: [24] i) the organic molecule must contain one or more terminal cation groups such as NH_3^+ that can interact with and hydrogen bond to the inorganic anion; ii) the organic cation must have appropriate width and shape (or the cross-sectional area of the molecule) that can fit into an area defined by the terminal halides from four adjacent corner-sharing octahedra; iii) the length of organic molecule can take a wide range of values compared to the width. The organic cation and the inorganic octahedra can each template the structural conformation of the other and consequently change materials properties.

To provide an informative summary of organic cations and inorganic frameworks, here we listed commonly used organic cations including their full names, abbreviations, and chemical formulas in Table I, and the experimentally synthesized hybrid perovskites including their crystal lattice type, space groups, and lattice parameters in Table II. Note that the abbreviation in Table I was chosen based on the following guidelines: i) whether it has been widely used; ii) whether it can reflect the meaning of the full name for the organic cation as briefly and precisely as possible; iii) avoid the usage of numbers to avoid confusions with the subscript number in the compound formula.

In addition, it is worth mentioning that an open-access database of the 2DHPs that includes over 500 compounds has been reported in a very recent work and is being regularly updated. [62] The database contains structural and chemical information and offers a useful data source for developing quantitative structure-property relationships for the 2DHPs, as shown by the developed machine learning models for the prediction of bandgaps and atomic partial charges in the Ref. [62].

Table I: List of organic cations in 2DHPs: abbreviation, full name, chemical formula, and compounds. The virtual compounds predicted from DFT calculations are marked with DFT.

Abbreviation	Full Name	Chemical Formula	Compound	Ref.
PD	AE <i>n</i> -(aminoethyl)piperidinium	$(C_5H_{10}-NH-(CH_2)_2-NH_3)^{2+}$	(AEPD)SnI ₄	[63]
QT	AE 5,5''-bis(aminoethyl)-2,2':5',2'':5'',2'''-quaterthiophene	$(NH_3-(CH_2)_2-(C_4H_4S)_2)^{2+}$	(AEQT)Pb{Cl,Br,I} ₄	[64]
TU	AE 2-•(Aminoethyl)isothiourea	$(NH_3(CH_2)_2SC(NH_2)_2)^{2+}$	(AETU)PbBr ₄	[65]
A	AL allylammonium	$(CH_2-CH-CH_2-NH_3)^+$	(ALA) ₂ (MA) _{n-1} Pb _n I _{3n-1}	[66]
MP	A <i>m</i> -(Aminomethyl)piperidinium	$(3-CH_2-NH-C_6H_9-NH_2)^{2+}$	(3AMP)(MA) _{n-1} Pb _n I _{3n+1}	[48]
		$(4-C_5H_9NH_2-NH_3-CMA)^{2+}$	(4AMP)(MA) _{n-1} Pb _n I _{3n+1}	[48]
MPD	A 2-(Ammoniomethyl)pyridinium	$(NH_3-CH_2-C_5H_5N)^{2+}$	(AMPD) ₂ Pb ₅ I ₂₂	[67]
	AP 4-Aminopyridine	$(H_2N-C_5H_4-NH)^{2+}$	(AP)PbBr ₄	[68]
A	AV 5-Aminovaleric Acid	$5-HOOC-(CH_2)_4-NH_3^+$	(AVA) ₂ PbI ₄	[69]
	BA Butylammonium	C ₄	(BA) ₂	[58,70]

			$H_9 NH_3^+$	$(MA)_{n-1} Pb_n I_{3n+1}$	
				$(BA)_2$	[71]
				$(MA)_{n-1} Sn_n I_{3n+1}$	
				$(BA)_2$	[72]
				$\{Ge, Sn, Pb\}I_4$	
ESBT	BA	5,5'-bis(ammoniummethylsulfanyl)-2,2'-bithiophene	$(NH_3^+ - (CH_2)_2 - S - (C_4H_2S))_2^{2+}$	$(BAESBT)PbI_4$	[73]
Z	BA	2,2'-Bi-aziridinium	$(NH_2 CH_2)_2^{2+}$	$(BAZ)SnI_4$ (DFT)	[74]
A	BD	1,4-Butanediammonium	$(NH_3^+ (CH_2)_4 NH_3^+)^{2+}$	$(BDA)PbI_4$	[75]
ECH	BA	1,4-bis(aminomethyl)cyclohexane	$(C_6H_{10} (CH_2)_2 (NH_3^+)_2)^{2+}$	$(BAECH)PbI_4$	[76]
M	BI	2,2'-Bi-imidazolium	$(C_3H_2(NH)_2 - C_3H_2(NH)_2)^{2+}$	$(BIM)SnI_4$ (DFT)	[74]
	BP	4,4'-Bi-pyridinium	$(C_5H_4NHC_5H_4NH)^{2+}$	$(BP)SnI_4$ (DFT)	[74]
PEA	Br-	2-(4-bromophenyl)ethanaminium	$BrC_6H_4 - C_2H_4 - NH_3^+$	$(Br-PEA)_2 (MA)_2 Pb_3 I_{10}$	[77]
A	BY	but-3-yn-1-ammonium	$CH_3 - C \equiv C - CH_2 - NH_3^+$	$(BYA)_2 PbBr_4$	[78]
	BZ	Benzimidazole	$C_7H_7N_2^+$	$(BZ)_2 Pb\{Cl, Br, I\}_4$	[79]
A	BZ	Benzylammonium	$C_6H_5 CH_2 NH_3^+$	$(BZA)_2 \{Pb, Sn\}I_4$	[80]

			⁺ ₃		
				(BZA) ₂	[81]
				PbCl ₄	
P	BZ	Benzylpiperazinium	(C ₆ H ₅ CH ₂ NHC ₄ H ₈ NH ₂) ²⁺	(BZP)PbCl ₄	[82]
N	CA	4-Chloroanilinium	4-Cl-C ₆ H ₄ NH ₃ ⁺	(CAN) ₂	[83]
				(CAN) ₂	[84]
				CuCl ₄	
A	CB	Cyclobutylammonium	C ₄ H ₇ NH ₃ ⁺	(CBA) ₂	[83]
A	CH	Cyclohexylammonium	C ₆ H ₁₁ NH ₃ ⁺	(CHA) ₂	[85]
				(CHA) ₂	[86]
				PbBr ₄	
				(CHA) ₂	[87]
				PbI ₄	
				(CHA) ₂	[88]
				{MA, Cs} _{n-1} Pb _n	
				I _{3n+1}	
E	CH	2-Cyclohexenylethanamine	C ₆ H ₉ (CH ₂) ₂ NH ₃ ⁺	(CHE) ₂	[89]
PEA	Cl-	2-(4-chlorophenyl)ethanaminium	ClC ₆ H ₄ -C ₂ H ₄ -NH ₃ ⁺	(Cl-PEA) ₂ (MA)	[77]
				Pb ₃ I ₁₀	
M	C	Cyclohexylmethanamine	C ₆ H ₁₁ CH ₂ NH ₃ ⁺	(CM) ₂	[89]
				PbCl ₄	
	CA	Cyclopropylammonium	C ₃ H ₅ NH ₃ ⁺	(CA) ₂	[83]
				PbI ₄	
A	CP	Chloropropylammonium		(CPA) ₄	[90]

			$\text{Cl}(\text{CH}_2)_3\text{NH}_3^+$	AgBiBr_8	
E	CP	Cyclopentylammonium	$\text{C}_5\text{H}_9\text{NH}_3^+$	$(\text{CPE})_2\text{PbI}_4$	[83]
MA	CB	cis-1,3-Bis(aminomethyl)cyclohexane	$(\text{C}_8\text{H}_{14}\text{NH}_3)_2^{2+}$	$(\text{CBMA})\text{PbBr}_4$	[91]
A	DD	Dodecyl diammonium	$(\text{NH}_3(\text{CH}_2)_{12}\text{NH}_3)^{2+}$	$(\text{DDA})\text{PbI}_4$	[92, 83]
	DA	Dodecylammonium	$\text{C}_{12}\text{H}_{25}\text{NH}_3^+$	$(\text{DA})_2\text{PbI}_4$	[83]
N	DA	1,5-Diammoniumnaphthalene	$(\text{NH}_3\text{C}_{10}\text{H}_6\text{NH}_3)^{2+}$	$(\text{DAN})\text{PbI}_4$	[93]
MA	D	Dimethylammonium	$(\text{CH}_3)_2\text{NH}_2^+$	$(\text{DMA})_7\text{Pb}_4\{\text{Cl}, \text{Br}\}_{15}$	[94]
MABA	D	4-Dimethylaminobutylammonium	$((\text{CH}_3)_2\text{NH})(\text{CH}_2)_4\text{NH}_3^+$	$(\text{DMABA})\text{PbBr}_4$	[95]
MAPA	D	3-(Dimethylamino)-1-propylamine	$((\text{CH}_3)_2\text{NH})(\text{CH}_2)_3\text{NH}_3^+$	$(\text{DMAPA})\text{PbBr}_4$	[95]
MEN	D	2-(Dimethylamino)-ethylammonium	$((\text{CH}_3)_2\text{NH})(\text{CH}_2)_2\text{NH}_3^+$	$(\text{DMEN})\text{PbBr}_4$	[95]
DEA	DT	2,2'-dithiodiethanammonium	$(\text{NH}_3(\text{CH}_2)_2\text{SS}(\text{CH}_2)_2\text{NH}_3)^{2+}$	$(\text{DTDEA})\text{PbI}_4$	[96]
	EA	Ethyleneammonium	$\text{CH}_3\text{CH}_2\text{NH}_3^+$	$(\text{EA})_4\text{PbCl}_{10}$	[97]

			$(EA)_4 Pb$ $3 Br_{10-x} Cl_x$	[98]
			$(EA)_2 PbI_4$ (DFT)	[99]
A	ED	Ethylenediammonium	$(NH_3(CH_2)_2 NH_3)^{2+}$	(EDA)SnI ₄ (DFT) [74]
				(EDA) ₂ PbI ₄ (DFT) [99]
BE	ED	2,2'-(Ethylenedioxy)- bis(ethylammonium)	$(NH_3(CH_2)_2 O(CH_2)_2 NH_3)^{2+}$	(EDBE)Pb{Cl, Br, I} ₄ [100]
MI	E	1-ethyl-3-methylimidazolium	$1-C_2H_5-3-CH_3-C_3H_3N_2^+$	(EMI) ₂ PbI ₄ (DFT) [99]
	FA	Formamidinium	$CH(NH_2)_2^+$	(FA,GA) PbI ₄ [101]
EA	FP	<i>m</i> -Fluorophenethylammonium	$C_6H_4F(CH_2)_2 NH_3^+$	(FPEA) SnI ₄ [102]
		(<i>m</i> = 2, 3, or 4)		(FPEA) ₂ PbI ₄ [103]
N	FA	4-Fluoroanilinium	$4-F-C_6H_4NH_3^+$	(FAN) ₂ CuCl ₄ [84]
EA	F-P	4-fluorophenylethylammonium	$FC_6H_4-C_2H_4-NH_3^+$	(F-PEA) (MA) ₂ Pb ₃ I ₁₀ [77]
PEA	F5-	perfluorophenethylammonium	$C_6F_5-C_2H_4$	(F5-PEA) ₂ PbI ₄ [104]

			$-\text{NH}_3^+$		
A	FS	2-(4-(3-fluoro)stilbenyl)ethan ammonium	FC $6 \text{H}_4 -(\text{CH})$ $2 -\text{C}_6 \text{H}_4 -\text{C}$ $2 \text{H}_4 -\text{NH}_3^+$	(FSA) ₂ (MA)Sn ₂ I ₇	[105]
	GA	Guanidinium	$\text{C}(\text{NH}_2)_3^+$	(FA,GA) 2PbI_4	[101]
				(GA)(MA) $)_n \text{Pb}_n \text{I}_{3n+1}$	[49]
	HA	Hexylammonium	C_6 $\text{H}_{13} \text{NH}_3^+$	(HA) ₂ (MA)Pb ₂ I ₇	[106]
				(HA) ₂ PbI_4	[107]
A	HD	n-Hexadecylammonium	C $16 \text{H}_{33} \text{NH}_3^+$	(HDA) ₂ PbI_4	[83]
A	HI	Histammonium	(C $5 \text{N}_3 \text{H}_{11}$) $2+$	(HIA){Pb, Sn}I ₄	[80]
	IA	isoamylammonium	$(\text{CH}_3)_2$ $\text{C}(\text{CH}_2)_2$ NH_3^+	(IA) (MA) ₂ Pb ₃ Br ₁₀	[108]
A	M	Methylammonium	$\text{CH}_3 \text{NH}_3^+$	(MA) ₂ $\text{Cu}\{\text{Cl}, \text{Br}\}_4$	[60]
				(MA) ₂ FeCl_4	[109,110]
				(MA) ₂ $\text{Pb}(\text{SCN})_2 \text{I}_2$	[111]
EDA	M	<i>n</i> '-Methylethane-1,2-diammonium	$(\text{CH}_3 \text{NH}_2)$ $(\text{CH}_2)_2 \text{NH}_3^+$ $3)^{2+}$	(MEDA)Pb{Br, Cl} ₄	[112]
M	MF	5-Methyl-2-furanmethanamine	$5-\text{CH}_3 -\text{OC}$ $4 \text{H}_2 -2-\text{CH}$ 2NH_3^+	(MFM) ₂ PbCl_4	[89]

	MI	1-methylimidazolium	$\text{CH}_3\text{C}_3\text{H}_4\text{N}_2^+$	(MI) ₂ PbI ₄ (DFT)	[99]
DA	MP	<i>n</i> ¹ -Methylpropane-1,3-diammonium	$(\text{CH}_3\text{NH}_2)(\text{CH}_2)_3\text{NH}_3^{2+}$	(MPDA)Pb{Br, Cl} ₄	[112]
EDA	MP	2-methylpentane-1,5-diammonium	$(\text{NH}_3-(\text{CH}_2)_2-\text{CH}-\text{CH}_2-\text{NH}_3)^{2+}$	(MPEDA)Pb{Cl, Br} ₄	[113]
TEA	M	2-(Methylthio)ethylamine	$\text{CH}_3\text{S}-(\text{CH}_2)_2-\text{NH}_3^+$	(MTEA) (MA) ₄ Pb ₅ I ₁₆	[114]
A	NE	2-(2-naphthyl)ethan ammonium	$\text{C}_{10}\text{H}_7-\text{C}_2\text{H}_4-\text{NH}_3^+$	(NEA) ₂ PbBr ₄	[115]
MA	N	1-(2-naphthyl)methan ammonium	$\text{C}_{10}\text{H}_7-\text{CH}_2-\text{NH}_3^+$	(NMA) ₂ PbBr ₄	[115]
A	OD	<i>n</i> -Octadecyl ammonium	$\text{C}_{18}\text{H}_{37}\text{NH}_3^+$	(ODA) ₂ PbI ₄	[83]
	OL	Oleyl ammonium	$\text{C}_{18}(\text{CH}_2)_7(\text{CH}_2)_8\text{NH}_3^+$	(OL) ₂ (MA) _{<i>n</i>-1} Pb _{<i>n</i>} {Cl, Br} _{3<i>n</i>+1}	[116]
	PA	Pentyl ammonium	$\text{C}_5\text{H}_{11}\text{NH}_3^+$	(PA) ₂ (MA)Pb ₂ I ₇	[106]
				(PA) ₂ PbI ₄ (DFT)	[99]
A	PD	Propane-1,3-diammonium	$(\text{NH}_3(\text{CH}_2)_3\text{NH}_3)^{2+}$	(PDA)(MA) _{<i>n</i>-1} Pb _{<i>n</i>} I _{3<i>n</i>+1}	[117]
MA	PD	1,4-phenylenedimethan ammonium	$(\text{NH}_3\text{CH}_2-\text{C}_6\text{H}_4-\text{CH}_2\text{NH}_3)^{2+}$	(PDMA)FA Pb _{<i>n</i>} I _{3<i>n</i>+1}	[118]

			$2 \text{NH}_3)^{2+}$		
A	PE	Phenylethylammonium	$\text{C}_6 \text{H}_5 \text{C}_2 \text{H}_4 \text{NH}_3^+$	(PEA) ₂ Pb{Cl, I, Br} ₄	[119]
				(PEA) ₂ (MA)Pb ₃ I ₁₀	[120]
				(PEA) ₂ (MA) _{n-1} Pb _n I _{3n+1}	[53]
				(PEA) ₂ (MA) _{n-1} Sn _n I _{3n+1}	[38]
				(PEA) ₂ Sn{I, Br} ₄	[121]
				(PEA) ₂ {Sn, Ge}I ₄	[122]
				(PEA) ₂ CuCl ₄	[123]
IM	PE	Phenylethanimidamide	$\text{C}_6 \text{H}_5 \text{NHCNHCH}_3^+$	(PEIM) PbI ₃	[75]
A	PM	Phenylmethan ammonium	$\text{C}_6 \text{H}_5 \text{CH}_2 \text{NH}_3^+$	(PMA) ₂ PbI ₄	[124]
				(PMA) ₂ PbCl ₄	[55]
A	PP	propyl phenyl ammonium	$\text{C}_6 \text{H}_5 \text{C}_3 \text{H}_7 \text{NH}_3^+$	(PPA) ₃ Pb ₂ I ₇	[125]
A	PT	phenyltrimethylammonium	$\text{C}_6 \text{H}_5 \text{-NH}_3^+$	(PTA) ₂ (MA) ₃ Pb ₄ I ₁₃	[126]
	PZ	Piperazinium	$(\text{C}_4 \text{H}_8 \text{NH}_2)^{2+}$	(PZ)PbCl ₄	[82]
MA	TH	2-thienylmethylammonium	$\text{C}_4 \text{H}_3 \text{SCH}_2^+$	(THMA) (MA)Pb ₂ I ₇	[127]

			$-\text{NH}_3^+$		
A	TF	3,4,5-Trifluoroaniline	$3,4,5\text{-F}_3\text{-C}_6\text{H}_2\text{NH}_3^+$	$(\text{TFA})_2\text{PbBr}_4$	[128]
M	TF	(Tetrahydrofuran-2-yl)methanamine	$\text{OC}_4\text{H}_7\text{CH}_2\text{NH}_2^+$	$(\text{TFM})_2\text{PbCl}_4$	[89]
M	TP	2-Thiophenemethylamine	$2\text{-S-C}_4\text{H}_4\text{CH}_2\text{NH}_3^+$	$(\text{TPM})_2\text{PbCl}_4$	[89]
A	TR	(carboxy)cyclohexyl-	$\text{HOOC-C}_6\text{H}_{10}\text{-CH}_2\text{-NH}_3^+$	$(\text{TRA})_2\text{SnI}_4$	[63]
	TU	Thiourea	$(\text{NHCSNH}_3)^{2+}$	$(\text{TU})\text{PbI}_4$	[129]

Fig. 2: An illustration of the structural evolution and experimental characterization of 2DHP. (a) Structural evolution of the RP-phase $(\text{BA})_2(\text{MA})_{n-1}\text{Ge}_n\text{Br}_{3n+1}$ ($n=1, 2,$ and 3), in which BA serves as barrier cations. (b-c) Structural characterization of $(\text{BA})_2(\text{MA})\text{Pb}_m\text{I}_{3m+1}$ ($m = 2, 3,$ and 4) from X-ray diffraction. Reproduced and adapted from Refs. [130] and [37].

Next, we review experimental characterization of the structural properties for several common types of 2DHPs: (i) perovskites containing long chain organic molecules and MA, (ii) perovskites containing aromatic ring molecules, (iii) perovskites containing MA only, (iv) perovskites containing dimethylammonium (DMA), and (v) newly discovered ACI perovskites.

(i) The first class contains long chain organic molecules with a chemical formula $\text{R}_2(\text{MA})_{n-1}\text{Pb}_n\text{I}_{3n+1}$, in which the large organic cation, R, refers to an aliphatic alkylammonium chain ($\text{C}_m\text{H}_{2m+1}\text{NH}_3$) with a length of m , such as the $\text{C}_4\text{H}_9\text{NH}_3$, where $m = 4$. One common class of 2DHPs is $(\text{BA})_2\text{MI}_4$ ($\text{M} = \text{Ge}, \text{Sn},$ and Pb), whose in-plane lattice constants increased as a function of the ionic radius of M cations, *i.e.*, from Ge to Sn and Pb. $(\text{BA})_2\text{GeI}_4$ was also found to have a higher degree of inorganic octahedra distortion than in Sn(II) and Pb(II) compounds due to stereochemical activity of the Ge(II) nonbonding electrons, and the stereoactivity increases in the order $\text{Pb(II)} < \text{Sn(II)} < \text{Ge(II)}$ as ligand bonding becomes more covalent.[72]

The 2DHP, $(\text{BA})_2(\text{MA})_{n-1}\text{Pb}_n\text{I}_{3n+1}$ was found to crystallize in an orthorhombic lattice for all n values, but in centrosymmetric for $n = 1$ and noncentrosymmetric for $n = 2-4$, and the compounds with an odd n value adopt a higher symmetry configuration compared to even n value compounds.[58] In this compound, the large BA cation requires a 7.8 \AA gap between the

perovskite layers and its $\text{NH}_3\text{CH}_2\text{CH}_2$ -head has a smaller degree of distortion than its CH_3CH_2 -tail, likely to be attributed to that the former is charged while the later is not. It was also found that the ratio between the spacer cation and the smaller organic cation can be adjusted to control the perovskite dimensionality. The 2DHPs, $(\text{C}_m\text{H}_{2m+1}\text{NH}_3)_2\text{PbI}_4$ ($m = 12, 14, 16, \text{ and } 18$), were also found with two reversible room-temperature phase transitions for each of them, due to the conformation of the hydrocarbon chains. and a shift of the inorganic layers.[131]

(ii) The second class contain aromatic or cyclic ring cations such as phenylethylammonium (PEA). $(\text{PEA})_2(\text{MA})_{n-1}\text{Pb}_n\text{Br}_{3n+1}$ ($n = 1-4$) crystals have distorted octahedral inorganic structures with a size of 6.3 \AA , [51] whose thin films were found to be a collection of their grains with a variety of n values instead of a single-phase.[53] This class of 2DHPs show a great variety of phases, mostly depending on the temperature. For example, $(\text{PEA})_2\text{CuCl}_4$ crystallizes in an orthorhombic phase with a space group of $Pbca$ below 340 K and $Cmca$ above 340 K; [123] $(\text{CA})_2\text{CuCl}_4$ ($\text{CA} = 4$ -chloroanilinium) crystallizes at 298K in the monoclinic phase, but undergoes a reversible phase transition at 150K from monoclinic to orthorhombic.[84] The Cd-based 2DHPs, $(\text{CHA})_2\text{CdBr}_4$ ($\text{CHA} = \text{cyclohexylammonium}$) crystallizes in a noncentrosymmetric and polar orthorhombic space group $Cmc2_1$. [85]

$(\text{HIA})\text{PbI}_4$ and $(\text{HIA})\text{SnI}_4$ ($\text{HIA} = \text{histammonium}$) crystallizes in a monoclinic phase with a space group $P2_1/n$, in which the divalent HIA cation was observed to bring layers close together, giving a certain 3D character to the structure. Interestingly, the inorganic frameworks of 2DHPs involving HIA and BZA are less distorted compared to the most single-layered 2DHPs, leading to slightly lower bandgaps. However, the inorganic layer of BZA compounds are still more distorted than that of HIA compounds due to the large M-I-M angle, which determines that the BZA compounds have overall larger bandgaps than the HIA compounds.[80] In $(\text{CBMA})\text{PbBr}_4$, the Pb-Br-Pb bond angles were found to strongly deviate from planar geometry due to hydrogen bonding between the organic ligands and the PbBr_4 octahedra.[91] The structures of several divalent aromatic ring contained perovskites have also been studied from DFT calculations, in which distorted structures were found in a staggered arrangement and the interlayer distances were small due to the strongly charged cations between organic layers.[74]

Fig. 3: A schematic of the structural derivation of 2DHP by cutting their parental cubic perovskite lattice along the planes (a) (100), (b) (110), and (c) (111). Reproduced and adapted with permission from Refs. [101].

Fig. 4: Crystal structures of 2DHPs: (a) corrugated α -(DMEN) PbBr_4 , (b) (DMAPA) PbBr_4 , and (c) (DMABA) PbBr_4 . Reproduced and adapted with permission from Refs. [95].

(iii) The third class contains the MA organic cation only, in which the separation between inorganic layers is not caused by a large organic cation. For example, in the lead-free 2DHPs, $(\text{MA})_2\text{CuX}_4$ ($\text{X} = \text{Cl and Br}$), the interlayer separation is achieved by steric hinderance effect that

was caused by the smaller ionic radii of the Cu^{2+} atoms.[60] $(\text{MA})_2\text{CuCl}_{0.5}\text{Br}_{3.5}$ crystallizes a layered structure with a spacing of 10 Å and crystallizes in the orthorhombic space group, as confirmed from X-ray diffraction (XRD). The Cu^{2+} inorganic layers also exhibit a highly distorted octahedral coordination due to Jahn-Teller distortion. The lattice parameters of these intermediate mixed-halide Cu-based perovskites are summarized in Table 2. $(\text{MA})_2\text{FeCl}_4$ crystallizes in a high-symmetry tetragonal phase above 335 K with a space group of $I4/mmm$ and elongated a and b lattice constants, while in the low-symmetry orthorhombic phase below 335 K with a space group of $Pccn$. [110]

In $(\text{MA})_2\text{Pb}(\text{SCN})_2\text{I}_2$, S-bonded SCN^- ligands in the *trans* position on the Pb octahedra separate the inorganic layers in a manner similar to that of a large organic cation in other 2D perovskites.[111] The first-principles calculations suggested that the SCN^- ions in this class of 2DHPs lead to shorten Pb–S bond lengths, more distorted octahedra, and more hydrogen bonds, hence improving the stability relative to the $(\text{MA})_2\text{PbI}_4$, along with strengthen Young's modulus and the resulting enhanced piezoelectric properties.[132] This work indicates that introducing SCN^- ions into the perovskite materials could serve one promising strategy to enhance the stability and mechanical properties of 2DHPs.

(iv) The fourth class are dimethyl- or diammonium-based 2DHPs, in which the inorganic monolayers are oriented in the (110) direction of their parental cubic perovskite lattice, different from the case of the former three classes of 2DHPs. Figure 3 shows the three derivations of 2DHPs by cutting their parental cubic perovskite lattice along the crystallographic planes (100), (110), and (111). In the 2DHP, α -(DMEN) PbBr_4 (DMEN = 2-(dimethylamino)ethylamine), its organic layers are composed of highly corrugated (110)-oriented layers,[95] see Figure 4a. As a comparison, the structures of monoclinic (DMAPA) PbBr_4 (DMAPA = 3-(dimethylamino)-1-propylamine) and orthorhombic (DMABA) PbBr_4 (DMABA = 4-dimethylaminobutylamine) which belong to conventional (100)-oriented family are shown in Figure 4b and 4c.

In addition to dimethyl cations, diammonium cations can also form similar structures, such as the (001) monoclinic perovskite (MPDA) PbBr_4 (1, MPDA = N^+ -methylpropane-1,3-diammonium), the corrugated (110) orthorhombic perovskite (MEDA) PbBr_4 (2, MEDA = N^+ -methylethane-1,2-diammonium), and monoclinic (EDBE) PbX_4 (EDBE = 2,2'-(ethylenedioxy)bis(ethylammonium), X = Cl, Br, I).[100 112, 133] The corrugated perovskite (FA,GA) PbI_4 (FA = formamidinium, GA = guanidinium) contains two large diammonium cations that alternate between interlayer spaces.[101] In $(\text{DMA})_7\text{Pb}_4\text{X}_{15}$ (X = Cl^- or Br^- , DMA = dimethylammonium), linear $\text{Pb}_4\text{X}_{15}^{7-}$ chains are linked together to form corrugated layers. The DMA cations were also found to be ordered under 100 K, but disordered at higher temperatures around 275 K.[94]

(v) The fifth class of 2DHPs is the ACI-phase perovskite that features two different alternating cations in the interlayer space. In 2017, Soe *et al.* first synthesized this class of 2DHPs, $(\text{GA})(\text{MA})_n\text{Pb}_n\text{I}_{3n+1}$, (GA = guanidinium, $\text{C}(\text{NH}_2)_3^+$).[49] In this compound, the GA^+ and MA^+ both serve as spacer cations which lead to an unique cation-ordering in the interlayer space. The ACI-phase can be considered as combining the layer-stacking features of both RP-phase and

DJ-phase structures. Compared to the RP-phase, the ACI structure has a higher crystal symmetry, leading to lower bandgaps and slightly reduced PL intensity compared to the RP-phase with the same perovskite layer thickness (n). It is noted that the GA^+ is the only cation that has been reported so far to form the ACI-phase structure with the MA^+ cations. In light of its enhanced properties,[49, 134] it is of great interests to explore the possibility to form novel ACI-phase 2DHPs using other small organic cations in future, from the perspectives of first-principles materials design first and followed by experimental synthesis.

Table II: List of 2DHPs: chemical formula, crystal system, space group, and lattice parameters at the measured temperature grouped by perovskite structure class.

Compound	T (K)	Crystal System	Space Group	a (Å)	b (Å)	c (Å)	β	Ref.
$(\text{BA})_2 \text{GeI}_4$	293	Orthorhombic	Pcmn	8.722	8.272	28.014	90	[72]
$(\text{BA})_2 \text{SnI}_4$	293	Orthorhombic	Pbca	8.837	8.619	27.562	90	[72]
$(\text{BA})_2 \text{PbI}_4$	293	Orthorhombic	Pbca	8.863	8.682	27.57	90	[72]
$(\text{BA})_2 (\text{MA})\text{Pb}_2 \text{I}_7$	293	Orthorhombic	Cc2m	8.947	8.859	39.347	90	[58]
$(\text{BA})_2 (\text{MA})_2 \text{Pb}_3 \text{I}_{10}$	293	Orthorhombic	C2cb	8.928	8.878	51.959	90	[58]
$(\text{BA})_2 (\text{MA})_3 \text{Pb}_4 \text{I}_{13}$	293	Orthorhombic	Cc2m	8.927	8.882	64.383	90	[58]
$(\text{BA})_2 (\text{MA})_4 \text{Pb}_5 \text{I}_{16}$	293	Orthorhombic	C2cb	8.905	77.013	8.931	90	[70]
$(\text{MA})_2 \text{CuCl}_4$		Monoclinic	P121/a1	7.257	7.35	9.69	111.2	[60]
$(\text{MA})_2 \text{CuCl}_2 \text{Br}_2$		Orthorhombic	Acam	7.319	7.328	19.134	90	[60]
$(\text{MA})_2 \text{CuClBr}_3$		Orthorhombic	Acam	7.397	7.369	19.322	90	[60]
$(\text{MA})_2 \text{CuCl}_{0.5} \text{Br}_{3.5}$		Orthorhombic	Acam	7.428	7.469	19.308	90	[60]
$(\text{MA})_2 \text{CuBr}_4$				7.801	7.624	19.129		[60]
$(\text{MA})_2 \text{FeCl}_4$	273	Tetragonal	I4/mmm	7.203	7.203	19.126	90	[110]
$(\text{MA})_2 \text{FeCl}_4$	383	Orthorhombic	Pccn	5.12	5.12	19.272	90	[110]
$(\text{MA})\text{Pb}(\text{SCN})_2 \text{I}$	298	Orthorhombic	Pnm2 ₁	18.58	6.267	6.466	90	[111]

²								
(PEA) ₂ (MA) ₂ Pb ₃ I ₁₀	100	Triclinic	P1	8.728	8.733	28.803	95.878	[54]
(PEA) ₂ CuCl ₄	100	Orthorhombic	Pbca	7.21	7.266	38.238	90	[123]
(PEA) ₂ CuCl ₄	370	Orthorhombic	Cmca		7.343	7.394	90	[123]
(FAN) ₂ CuCl ₄	150	Monoclinic	P2 ₁ /c		7.379	7.093	99.004	[84]
(CA) ₂ CuCl ₄	150	Orthorhombic	Pccn	7.374	32.069	7.161	90	[84]
(CA) ₂ CuCl ₄	298	Monoclinic	P2 ₁ /c		7.391	7.263	101.576	[84]
(CHA) ₂ CdBr ₄	300	Orthorhombic	Cmc2 ₁		8.673	8.605	90	[85]
(BZA) ₂ PbCl ₄	293	Orthorhombic	Cmc2 ₁	33.64	7.817	7.737	90	[81]
(BZA) ₂ PbBr ₄	293	Orthorhombic	Cmca		8.153	8.131	90	[81]
(BZA) ₂ PbI ₄	293	Orthorhombic	Pbca	9.156	8.689	28.776	90	[80]
(BZA) ₂ SnI ₄	293	Orthorhombic	Pbca	9.094	8.661	28.764	90	[80]
(HIA)PbI ₄	293	Monoclinic	P2 ₁ /n	8.916	20.034	8.993	91.875	[80]
(HIA)SnI ₄	293	Monoclinic	P2 ₁ /n	8.741	20.045	8.984	91.571	[80]
(CBMA)PbBr ₄	298	Orthorhombic	Pnma		24.457	7.979	90	[91]
(3AMP)PbI ₄	293	Monoclinic	P2 ₁ /c	8.673		18.4268	20.452	99.306
(3AMP)(MA) ₃ Pb ₄ I ₁₃	293	Cubic	Ia	8.863	8.869	58.842	90	[48]
(4AMP)PbI ₄	293	Monoclinic	Pc	10.5	12.543	12.529	89.984	[48]
(4AMP)(MA) ₃ Pb ₄ I ₁₃	293	Cubic	Ia	8.859	8.857	58.915	90	[48]
α-(DMEN)PbBr ₄	293	Orthorhombic	Pbca		11.782	23.680	90	[95]
β-(DMEN)PbBr ₄	293	Monoclinic	P2 ₁ /c		11.982	18.724	90.44	[95]
(DMAPA)PbBr ₄	293	Monoclinic	P2 ₁ /c		11.735	12.127	111.53	[95]
(DMABA)PbBr ₄		Orthorhombic	Aba2		23.962	12	90	[95]

	293			41.685				
(MEDA)PbBr ₄	100	Orthorhombic	P2 ₁ 2 ₁ 2 ₁	6.076	8.393	23.743	90	[112]
(MPDA)PbBr ₄	100	Monoclinic	P2 ₁ /c	8.316	8.316	20.118	101.695	[112]
(EDBE)PbCl ₄	100	Monoclinic	C2	7.732	7.542	13.293	102.481	[100]
(EDBE)PbBr ₄	100	Monoclinic	P2 ₁ /c	6.092	28.78	8.886	91.852	[100]
(EDBE)PbI ₄	100	Monoclinic	Aba2	6.494	29.461	9.267	91.777	[100]
[Ni(OPD) ₂ (ACN) ₂] _n -[PbI ₄] _n	293	Monoclinic	P2 ₁ /c	13.981	7.888	19.746	95.303	[135]
(FA,GA)PbI ₄	298	Monoclinic	C2/m	26.948	12.819	14.408	109.941	[101]
(GA)(MA)PbI ₄	293	Orthorhombic	Imma	6.642	12.458	18.826	90	[49]
(GA)(MA) ₂ Pb ₂	293	Orthorhombic	Bmm2	6.373	12.544	31.376	90	[49]
(GA)(MA) ₃ Pb ₃	293	Orthorhombic	Imma	6.352	12.438	43.970	90	[49]

III. Synthesis

Thin films are one critical component of high-performance devices such as solar cells and light-emitting diodes (LEDs). The quality of a thin film is mainly determined by its fabrication approach that could significantly influence its optoelectronic properties.[4, 9, 54] Compared to 3DHPs such as (MA)PbI₃, which often requires complex fabrication methods to achieve high-quality films,[4, 3, 136] the 2DHP can form ultra-smooth thin films with high surface coverage, fine texture, and few grain boundaries from a simple one-step spin-coating approach.[37]

A variety of different approaches such as the solution-based spin coating method, vapor-phase synthesis method, colloidal growth method, and exfoliation method have been used for synthesizing 2D materials. The vapor-phase (or gas-phase) synthesis is commonly used for traditional inorganic materials synthesis and generally requires high-temperature operations, and thus unsuitable for the hybrid organic-inorganic perovskite materials. [46] The colloidal growth method is a well-established wet-chemical precipitation process and traditionally used for synthesizing inorganic nanocrystals (quantum dots) with varying compositions, sizes, and shapes.[137] The mechanical exfoliation was also tried to produce thin sheets of 2DHPs, such as

(BA)₂PbBr₄, [59] (BA)₂PbI₄, [138] (PEA)₂PbI₄, [61] and (BA)₂(MA)_{n-1}Pb_nI_{3n+1}, [139] though this approach often produces non-uniform 2DHP films. For instance, the mechanical exfoliation yielded very thick flakes while the solvent exfoliation yielded randomly shaped particles. Moreover, the monolayer-thick particles produced from this approach were found very small (less than 1 μm), suggesting that the hybrid perovskite layers are mechanically brittle. [59] It is worth mentioning that the mechanical exfoliation method is rather appropriate for the investigation of fundamental materials properties of 2DHPs but might not be suitable for large-scale production due to the difficulty of the size and thickness control. [46]

Compared to the vapor-phase and colloidal growth methods, the solution-based spin coating method has significant advantages including its simplicity, low-cost fabrication, and particularly low-temperature operations, which make it most appropriate for the film synthesis of 2DHPs. [12, 37, 38, 54, 55, 80, 87, 107, 140–143] Herein we mainly focus on the solution-based spin coating approach and present a comprehensive review for the whole process, along with its remarkable features. An introduction of the other methods for the synthesis of 2DHPs can be found in several recent review articles. [30, 42, 46, 144, 145]

Fig. 5: Synthesis routes of hybrid halide perovskites. (a) A schematic of the spin-coating procedure for MA_nPbI₃, in which PbI₂ solution is firstly spin-coated on the mesoporous TiO₂ film, and then MAI solution is spin-coated on PbI₂. (b) A self-doping approach to prepare 2DHP, (BA)₂(MA)_{n-1}Pb_nBr_{3n+1}, which contains two sequential steps: (1) synthesis of two-dimensional (BA)₂PbBr₄ perovskite via a ternary solvent approach and (2) transformation of (BA)₂PbBr₄ into (BA)₂(MA)_{n-1}Pb_nBr_{3n+1} perovskites via chemical vapor deposition of MABr. The illustration of the structural transformation in the second step is shown in (3). Reproduced and adapted with permission from [12] and [146].

Figure 5a shows a schematic illustration of the solution-based spin-coating approach for the synthesis of thin films of hybrid perovskite. The halide perovskite solutions are typically prepared by dissolving organic and inorganic precursors in the dimethylformamide (DMF) solvent. [37, 51, 55, 87, 119, 142, 147] For example, Kanatzidis' research team synthesized RP-type 2DHP, (BA)₂(MA)_{n-1}Pb_nI_{3n+1} (n=1-4), from a stoichiometric reaction between PbI₂, MAI, and BA, and fabricated high-quality thin films through spin-coating perovskite solutions on mesoporous TiO₂ substrates. [37] Compared to the two-step synthesis process for MA_nPbI₃ (Figure 5a), all the thin films of (BA)₂(MA)_{n-1}Pb_nI_{3n+1} in this work were fabricated by a one-step deposition method, with the inorganic [Pb_nI_{3n+1}]⁻ layers perpendicular to the substrate. It is worth mentioning that the 2D thin films were formed immediately after the spin-coating process without annealing steps, indicating the easiness of this approach and great compatibility with flexible substrates. [37]

To synthesize the high-quality thin films of 2DHPs, the perovskite solutions can also be prepared by dissolving perovskite powders in the solvent, and it is even necessary particularly when the perovskite precursor solution plays a critical role in the final film quality. [38] For example, Kanatzidis' research team found that only using the pure bulk materials as film precursors can ensure the formation of clean film of desired 2DHPs, *i.e.*, (BA)₂(MA)_{n-1}Sn_nI_{3n+1}

($n=1-5$). [38] Interestingly, the research team also found that the orientation of the thin film growth on a substrate is determined by the solvent used to dissolve the bulk perovskites: the thin film grows parallel to the planar substrate if dimethyl sulfoxide (DMSO) is used and perpendicular if DMF is used. By using the spin-coating approach, some other 2DHPs have been fabricated, such as $(\text{PEA})_2 (\text{MA})_{n-1} \text{Pb}_n \text{Br}_{3n+1}$, [51–54, 148, 149] $(\text{MA})_2 \text{Pb}(\text{SCN})_2 \text{I}_2$, [142] $(\text{CHA})_2 \text{PbBr}_4$ [86], $(\text{CHA})_2 \text{PbI}_4$, [87] $(\text{PEA})_2 \text{PbZ}_{4(1-x)} \text{Y}_{4x}$ and $(\text{PEA})_2 \text{PbZ}_{3(1-x)} \text{Y}_{3x}$, [119] and $(\text{R}-(\text{CH}_2)_n \text{NH}_3)_2 \text{PbX}_4$, [55] where X, Y, and Z are halogen ions such as I, Br, and Cl.

Co-solvents can be used for improving the crystallization of the thin films of 2DHPs and promoting the synthesis process. For example, a ternary co-solvent that contains dimethylformamide (DMF), chlorobenzene (CB), and acetonitrile has been used to prepare the thin 2DHP $(\text{BA})_2 \text{PbBr}_4$ and its derivatives. [59, 150] The three solvents have their own roles: the polar organic DMF was used to dissolve the PbBr_4 -based inorganic materials; the CB reduces the solubility of $(\text{BA})_2 \text{PbBr}_4$ in DMF and promotes crystallization; and acetonitrile facilitates the formation of the ultrathin 2DHP sheets. The same technique based on the DMF-CB-acetonitrile ternary solvent were also employed to synthesize other 2DHPs such as $(\text{MA})_2 \text{Pb}(\text{SCN})_2 \text{I}_2$ [151] and $(\text{TFA})_2 (\text{MA})_{n-1} \text{Pb}_n \text{Br}_{3n+1}$ ($\text{TFA} = 3,4,5$ -trifluoroaniline). [128]

In addition to the simplicity, the spin-coating method also allows for some flexibility to the growth of 2DHPs, enabling a control of crystal structure and grain morphology, which includes (i) layer orientation, [152] (ii) grain size, [39] (iii) composition, [60] and (iv) dimensionality, [69, 153] which are discussed as below.

First, the layer orientation of 2DHP thin films can be controlled by varying the solvent or spin speed, as mentioned above in the case of $(\text{BA})_2 (\text{MA})_{n-1} \text{Sn}_n \text{I}_{3n+1}$. [38] Similar phenomenon also occurs in the case of $(\text{BA})_2 (\text{MA})_{n-1} \text{Pb}_n \text{I}_{3n+1}$ ($n=1-4$), [37] with the inorganic layers perpendicular to the substrate when the DMF solvent was used, which favors the charge transport and is thus beneficial for the optoelectronic applications such as solar cells. Hamaguchi *et al.* synthesized thin films of 2DHPs, $(\text{HA})_2 (\text{MA})\text{Pb}_2 \text{I}_7$ and $(\text{HA})_2 (\text{FA})\text{Pb}_2 \text{I}_7$, using the standard spin-coating method, and by increasing the spin speed, and found that the proportion of perpendicularly orientated layers increases. [152] Venkatesan *et al.* demonstrated that the orientation of the inorganic layers in $(\text{BA})_2 (\text{MA})_{n-1} \text{Pb}_n \text{I}_{3n+1}$ could be gradually changed from parallel to perpendicular to the substrate with increasing dimensionality n . [154] All these works suggest that the spin-coating approach offers one important tool to manipulate the orientation of the 2DHP thin films, which is critical for fundamental studies for the optoelectronic properties and applications.

Second, crystal size and grain morphology can be controllable via the solvent evaporation temperature. The hot casting technique involves spin-coating on a heated substrate, leading to perovskites of near-single-crystalline quality. The high quality of perovskites provides channels with fast charge transport, allowing charge carriers to travel across electrodes without inhibition of insulating spacer layers. [39] Sun *et al.* found that longer annealing times facilitate the decomposition of small- n quantum wells and the formation of large- n quantum wells in mixed dimensionality perovskite films. [143] Raghavan *et al.* showed that millimeter-sized crystals of $(\text{BA})_2 (\text{MA})_{n-1} \text{Pb}_n \text{I}_{3n+1}$ can be synthesized via a slow evaporation at a constant temperature, and these crystals demonstrated high crystallinity, phase purity, and spectral uniformity. [155] A

Cd-based 2DHP, $(\text{CHA})_2 \text{CdBr}_4$ was also synthesized in a similar fashion.[85]

Along the same line, the morphology of 2DHPs thin films can also be tuned from its crystallization rate, which can be realized via solvent engineering. For example, Soe *et al.* synthesized compact thin films of $(\text{GA})(\text{MA})_n \text{Pb}_n \text{I}_{3n+1}$ with excellent surface coverage using a chlorobenzene antisolvent dripping method.[49] This technique promotes faster perovskite crystallization by expediting the solvent removal during the spin coating process.[9, 156]

Third, the chemical composition of 2DHPs can be varied by changing the precursor components during the perovskite crystal synthesis. For example, Cortecchia *et al.* fabricated 2D Cu-based, Cl/Br mixed halide perovskites by stoichiometrically mixing, then crystallizing perovskite powders in ethanol.[60] Zhou *et al.* introduced a ternary organic cation to form $(\text{BA})_2 (\text{MA,FA})_3 \text{Pb}_4 \text{I}_{13}$ perovskite films by replacing MAI with FAI in the stoichiometric reaction between PbO, MAI, and BAI. Interestingly, at 20% FA, crystal grains increased from several hundred nanometers to several micrometers; at 40% and higher amounts of FA, grain size increased in the films, but the density decreased, and more pinholes and cracks formed; and at 60% FA, microparticles appeared on the surface and the film roughness increased three times compared to 40% FA. These results suggest that changing the chemical compositions is also one effective way to tune the grain size and grain morphology.[157]

Fourth, the dimensionality can be controlled with the addition of an MAI immersion step. For instance, Koh *et al.* synthesized the quasi-2DHP, $(\text{IC}_2 \text{H}_4 \text{NH}_3)_2 (\text{MA})_{n-1} \text{Pb}_n \text{I}_{3n+1}$, with increased dimensionality, using the standard spin-coating method for the pure 2D components, followed by immersion in a $\text{CH}_3 \text{NH}_3 \text{I}$ dipping solution for 1-5 minutes.[153] Chen *et al.* reported a so-called “self-doping” approach to synthesize homologous $(\text{BA})_2 (\text{MA})_{n-1} \text{Pb}_n \text{Br}_{3n+1}$ using the ultrathin $(\text{BA})_2 \text{PbBr}_4$ as the template via MABr doping, see Figure 5b.[146] In this work, the $(\text{BA})_2 \text{PbBr}_4$ template was synthesized first using the solution-based approach, and upon MABr doping, the thickness of $(\text{BA})_2 (\text{MA})_{n-1} \text{Pb}_n \text{Br}_{3n+1}$ shrank down to 4.2 nm.

Alongside dimensionality control, 2D/3D junctions can also be formed by a slow drying process of a 2D/3D perovskite precursor mixture. Grancini *et al.* used this method to synthesize 2D/3D $(\text{AVA})_2 \text{PbI}_4 / (\text{MA}) \text{PbI}_3$ perovskite junctions by mixing the precursors at different molar ratios (0-3-5-10-20-50%).[69] The mixed solution was deposited on and infiltrated in an inert ZrO_2 scaffold followed by a slow drying-process, allowing the components to be reorganized before solidification. Similarly, Lin *et al.* created 2D/3D stacking structures by spin-coating solutions of BA and BAI on top of 3D perovskite layers; and the BA treatment led to a smoother 2D layer with better coverage compared to BAI treatment.[140] A blend of quasi-2DHPs and 3DHPs can also be created by dissolving weight ratios of perovskites solutions in DMF then spin-coating.[116] 2DHP-based heterojunctions and interfaces can also be found in a recent review article.[158]

Table III: Bandgaps (eV) of several 2DHPs as a function of dimensionality, n . ^a Denotes the calculations with spin-orbit coupling.

Compound	1	2	3	4	n	∞	Ref
Experimental							

$(\text{BA})_2(\text{MA})_{n-1}\text{Pb}_n\text{I}_{3n+1}$	2.39	2.14	2.02				[147]
$(\text{BA})_2(\text{MA})_{n-1}\text{Pb}_n\text{I}_{3n+1}$	2.24	1.99	1.85	1.6		1.52	[37]
$(\text{BA})_2(\text{MA})_{n-1}\text{Pb}_n\text{I}_{3n+1}$	2.42	2.15	2.04	1.92	1.85		[159]
$(\text{BA})_2(\text{MA})_{n-1}\text{Pb}_n\text{I}_{3n+1}$	2.43	2.17	2.03	1.91		1.5	[58]
$(\text{BA})_2(\text{MA})_{n-1}\text{Sn}_n\text{I}_{3n+1}$	1.83	1.64	1.5	1.42	1.37	1.2	[38]
$(\text{PEA})_2(\text{MA})_{n-1}\text{Pb}_n\text{I}_{3n+1}$	2.4	2.2	2				[160]
$(\text{PEA})_2(\text{MA})_{n-1}\text{Pb}_n\text{I}_{3n+1}$	2.41	2.21	2.18	1.88	1.82	1.68	[53]
$(\text{PEA})_2(\text{MA})_2\text{Pb}_3\text{I}_{10}$			2.1				[54]
$(3\text{AMP})(\text{MA})_{n-1}\text{Pb}_n\text{I}_{3n+1}$	2.23	2.02	1.92	1.87	1.8	1.59	[48]
$(4\text{AMP})(\text{MA})_{n-1}\text{Pb}_n\text{I}_{3n+1}$	2.38	2.17	1.99	1.89	1.8	1.59	[48]
$(\text{GA})(\text{MA})_n\text{Pb}_n\text{I}_{3n+1}$	2.27	1.99	1.73				[49]
DFT							
$(\text{PEA})_2(\text{MA})_{n-1}\text{Pb}_n\text{I}_{3n+1}$	2.31	2.17	1.95				[160]
$(\text{PEA})_2(\text{MA})_{n-1}\text{Pb}_n\text{I}_{3n+1}$	1.43	1.2	0.91 ^a				[160]
$(\text{BA})_2(\text{MA})_{n-1}\text{Pb}_n\text{I}_{3n+1}$	1.99		1.78	0.96			[58]
$(\text{BA})_2(\text{MA})_{n-1}\text{Pb}_n\text{I}_{3n+1}$	2.0		1.7			1.2	[39]
$(\text{GA})(\text{MA})_n\text{Pb}_n\text{I}_{3n+1}$	1.12	0.75	0.12				[49]

Table IV: Experimental bandgaps (eV) of several 2DHPs as a function of composition, x .

Compound	0	0.125	0.25	0.5	0.75	0.875	1	Ref
$(\text{PEA})_2 \text{Ge}_{x-1} \text{Sn}_x \text{I}_4$	2.13	2.09	2.04	1.95				[122]
$(\text{PEA})_2 \text{SnI}_{4x} \text{Br}_{4(x-1)}$	2.66		2.47	2.28	2.13		1.97	[121]
$(\text{HIA})_2 \text{Pb}_{x-1} \text{Sn}_x \text{I}_4$	2.05		1.78	1.76	1.74		1.67	[80]
$(\text{BZA})_2 \text{Pb}_{x-1} \text{Sn}_x \text{I}_4$	2.18		1.86	1.84	1.82		1.89	[80]
$(\text{MA})_2 \text{CuCl}_{4(x-1)} \text{Br}_{4x}$	2.48			2.12	1.9	1.8		[60]

Table V: Bandgaps (eV) of several single layer 2DHPs.

Compound	Bandgap (eV)	Ref	Compound	Bandgap (eV)	Ref
Experimental					
$(\text{DA})\text{PbI}_4$	2.75	[83]	$(\text{CHE})\text{PbCl}_4$	3.64	[55]
$(\text{HDA})\text{PbI}_4$	2.98	[83]	$(\text{BZA})_2 \text{PbCl}_4$	3.65	[81]
$(\text{ODA})\text{PbI}_4$	2.98	[83]	$(\text{PEA})_2 \text{PbCl}_4$	3.64	[55, 119]
$(\text{CA})\text{PbI}_4$	3.25	[83]	$(\text{PEA})_2 \text{PbBr}_4$	3.07	[119]
$(\text{CHE})\text{PbI}_4$	2.87	[83]	$(\text{PEA})_2 \text{PbI}_4$	2.4	[119, 141]
$(\text{CA})\text{PbI}_4$	3.04	[83]	$(\text{PEA})_2 \text{PbI}_4$	2.49	[83]
$(\text{CBA})\text{PbI}_4$	2.88	[83]	$(\text{MA})_2 \text{Pb}(\text{SCN})_2 \text{I}_2$	2.04	[142]
$(\text{CPE})\text{PbI}_4$	2.86	[83]	$(\text{MA})_2 \text{Pb}(\text{SCN})_2 \text{I}_2$	1.77	[111]
$(\text{DDA})\text{PbI}_4$	2.99	[83]	$[\text{Ni}(\text{opd})_2 (\text{acn})_2]_n - [\text{Pb}_4 \text{I}_{10}]_n$	2.67	[135]
$(\text{CM})\text{PbCl}_4$	3.7	[55]	$(\text{BDA})\text{PbI}_4$	2.64	[75]
$(\text{PMA})\text{PbCl}_4$	3.7	[55]	$(\text{PEIM})\text{PbI}_3$	2.73	[75]
$(\text{TPM})\text{PbCl}_4$	3.7	[55]	$\alpha - (\text{DMEN})\text{PbBr}_4$	3	[95]
$(\text{TFM})\text{PbCl}_4$	3.77	[55]	$(\text{DMAPA})\text{PbBr}_4$	2.88	[95]

(MFM)PbCl ₄	3.79	[55]	(DMABA)PbBr ₄	2.85	[95]
DFT					
(MA) ₂ Pb(SCN) ₂ I ₂	1.53	[50]	(BZA) ₂ PbCl ₄	3.34	[81]
(MA) ₂ Pb(SCN) ₂ I ₂	2.06	[142]	(BZA) ₂ PbI ₄	1.42	[80]
(BDA)PbI ₄	2.01	[75]	(BZA) ₂ SnI ₄	1.33	[80]
(PEIM)PbI ₃	2.91	[75]	(HIA)PbI ₄	1.34	[80]
(EDBE)PbI ₄	2.83	[161]	(HIA)SnI ₄	1.14	[80]

IV. Properties

In this section, we reviewed and discussed related electronic, optical, and energetic properties of 2DHPs. The layered structural characteristics of 2D materials strongly affect their stability and electronic properties such as charge carrier transport and bandgap. Some common findings of 2DHPs include bandgap tunability through adjusting layer thickness or compositions, charge carrier mobility anisotropy, excellent light absorption and emission properties, and relatively high materials stability.

A. Bandgap

Bandgap is one of the most important material parameters for optoelectronic applications. The 2DHPs' bandgaps have been extensively studied via light absorption and PL spectra. Tables 3, 4, and 5 summarized 2DHPs' bandgaps. Herein we review two major trends of bandgaps as a function of structural dimensionality and composition as well as the experimental determination of bandgaps as below.

First, the 2DHPs' bandgaps generally increase as the dimensionality decreases.[37, 38, 58, 159] Figure 6 shows the variations of bandgaps of (BA)₂(MA)_{n-1}Pb_nI_{3n+1} from 1.52 ($n = \infty$) to 2.24 eV ($n = 1$) via PL spectra measurements.[37] Similar observations were also reported by Stoumpos *et al.*, in which the bandgaps range from 1.5 ($n = \infty$) to 2.43 eV ($n = 1$) with intermediate values of 1.91 ($n = 4$), 2.03 ($n = 3$), and 2.17 eV ($n = 2$). [58] Note that the bandgap inversely correlates with the dimensionality regardless of the materials compositions of 2DHPs. For instance, the bandgaps of (PEA)₂(MA)_{n-1}PbI_{3n+1} range from 2.41 ($n = 1$) to 1.68 eV ($n = \infty$),[53] and Sn-based RP-type 2DHPs also demonstrate a similar trend.[38] The feature of bandgap tunability allows for enhanced functional applications in the novel optoelectronic devices including electro-optical modulators,[162] p-n junctions, transistors, photodiodes, and lasers.[163]

Fig. 6: Optical bandgaps of (a) bulk and (b) spin-coated TiO₂-perovskite thin films of the MA PbI₃ and (BA)₂(MA)_{n-1}Pb_nI_{3n+1} with $n=1, 2, 3, 4$, and ∞ . Reproduced with permission from [37].

Figure 7: Calculated projected-band structures of 2D $(\text{BA})_2(\text{MA})_{n-1}\text{Ge}_n\text{I}_{3n+1}$ and 3D MAGeI_3 perovskites, (a) $n=1$, (b) $n=2$, (c) $n=3$, and (d) $n=\infty$, along the Γ (0,0,0)-X(0.5,0,0)-S(0.5,0.5,0)-Y(0,0.5,0)- Γ (0,0,0)-Z(0,0,0.5)-R(0.5,0.5,0.5) path through the first Brillouin zone. The Fermi level is set to be zero and indicated by the red horizontal dash line. The relative contribution of Ge and I are marked by color, in which green (red) corresponds to the state originating from Ge (I). Reproduced and adapted from [130]. with permission from The Royal Society of Chemistry.

2DHPs typically exhibit wider bandgaps than 3DHPs, and the changing trend of bandgaps as a function of the thickness of inorganic layers can also be well predicted from first-principle computational studies. [54, 164, 165] In the previous first-principles studies of $(\text{BA})_2(\text{MA})_{n-1}\text{Ge}_n\text{I}_{3n+1}$, [130] we found that bandgaps decrease with increasing n values, ranging from 1.88, 1.83, 1.69 to 1.57 eV for $n = 1, 2, 3$, and ∞ , as shown in Figure 7. The calculated density of states (DOS) shows that the conduction band (CB) is mainly composed of Ge $4p$ states while the valence band (VB) is mainly composed of I $5p$ states, neither having any contribution from the organic molecules near the band edges. The calculated bandgaps of $(\text{BA})_2(\text{MA})_{n-1}\text{Pb}_n\text{I}_{3n+1}$ range from 1.2 (bulk) to 2.0 eV (monolayer), [39] comparable to the experimental values of 1.52 (bulk) to 2.24 eV (monolayer). [37] Peng *et al.* calculated the bandgaps of $(\text{PEA})_2(\text{MA})_{n-1}\text{Pb}_n\text{I}_{3n+1}$ to be 2.31 ($n = 1$), 2.17 ($n = 2$), and 1.95 eV ($n = 3$) without spin-orbit coupling, in good agreement with their experimental findings, while 1.43 ($n = 1$), 1.20 ($n = 2$), and 0.91 eV ($n = 3$) with spin-orbit-coupling. [160] Grancini *et al.* carried out first-principles calculations for the 2D/3D perovskite interface, $(\text{AVA})_2\text{PbI}_4/(\text{MA})\text{PbI}_3$, and found that at the $(\text{AVA})_2\text{PbI}_4/(\text{MA})\text{PbI}_3$ junction, there is a 0.14 eV CB upshift which induces a 0.09 eV larger interface gap compared to the 3D bulk, consistent with their experimentally observed 0.13 eV PL blue shift. [69] A large bandgap of 2DHPs opens the opportunity for novel applications in power devices, short-wavelength LEDs, [166] and high efficiency tandem solar cells. [167]

Second, the bandgaps can be tuned through selection of the halide anions, large organic cations, and metal cations. A more electronegative halide anion generally leads to a larger bandgap, and vice versa. For example, Cortecchia *et al.* demonstrated bandgap tunability of Cu-based perovskites, $(\text{MA})_2\text{CuCl}_x\text{Br}_{4-x}$, through Cl/Br ratio modification from DFT calculations, [60] in which the calculated bandgaps range from 3.09 to 3.00, to 2.88, and to 2.86 eV for $x = 4, 2, 1$, and 0.5, respectively. The bandgaps of mixed halide perovskites, $(\text{PEA})_2\text{PbZ}_{4(1-x)}\text{Y}_{4x}$ ($Z, Y = \text{Cl, Br, or I}$), can be tuned from 2.4 to 3.1 and 3.7 eV through changing compositions of anions. [121] In contrast, the bandgaps of $(\text{PEA})_2\text{Sn}_x\text{Br}_{4-x}$ decrease with increasing I concentrations. [121] Fraccarollo *et al.* calculated bandgaps of $(\text{BIM})\text{SnI}_4$ and $(\text{BP})\text{SnI}_4$ with values around 1.34-1.78 eV using DFT calculations by including SOC and GW effects, and attributed the low bandgap to the degenerate levels at the bottom of the conduction bands that are strongly localized in the interlayer space. [99]

The bandgaps can be tuned by partially substituting inorganic and/or organic cations. The bandgap of $(\text{PEA})_2\text{Ge}_{1-x}\text{Sn}_x\text{I}_4$ ($x = 0-0.5$) decreases almost linearly with increasing Sn

concentrations.[122] Similarly, the bandgaps of $(\text{HIA})\text{Pb}_{1-x}\text{Sn}_x\text{I}_4$ and $(\text{BZA})_2\text{Pb}_{1-x}\text{Sn}_x\text{I}_4$ were also found to decrease with increasing Sn concentration, with the lowest bandgap of 1.74 eV at an intermediate value of $x = 0.75$ for $(\text{BZA})_2\text{Pb}_{1-x}\text{Sn}_x\text{I}_4$. [80] Moreover, the bandgap decrease as the M–I–M angle approaches 180° , ranging from 2.18 eV for $(\text{BZA})_2\text{PbI}_4$ to 2.05 eV for $(\text{HIA})\text{PbI}_4$. Zhang *et al.* tuned the bandgap of PbCl_4 -based perovskites from 3.76 eV to 3.64 eV by using different large organic cations such as cyclohexylmethanamine (CM, 3.7 eV), phenylmethanamine (PM, 3.7 eV), 2-thiophenemethylamine (TPM, 3.7 eV), (tetrahydrofuran-2-yl)methanamine (TFM, 3.77 eV), 5-methyl-2-furanmethanamine (MFM, 3.79 eV), 2-cyclohexenylethanamine (CHE, 3.64 eV), and PEA (3.64 eV).[55] However, it should be noted that while the bandgap can be varied via the choice of the large organic cation, the bandgaps do not involve the organic orbitals directly.[168] An accurate argument is that the large organic cation can indirectly influence the bandgap via the geometric distortions of the inorganic octahedra, as shown from DFT calculations.[169]

There are two types of bandgaps: direct and indirect. A direct bandgap semiconductor has the conduction band minimum (CBM) and the valence band maximum (VBM) located at the same k -vector in the Brillouin zone, allowing for photon absorption and emission without a change in the momentum. Conversely, an indirect bandgap requires a change in the momentum for photon emission and absorption.[170] Semiconductors with direct bandgaps are often preferred because they have higher photon absorption rate.[171, 172] Many 2DHPs were characterized with a direct bandgap.[75, 138, 142] For example, $(\text{BA})_2\text{PbI}_4$ has a direct bandgap of 2.4 eV; [138] $[\text{Ni}(\text{opd})_2(\text{acn})_2]_n\text{-}[\text{Pb}_4\text{I}_{10}]_n$ (opd = o-Phenylenediamine, $\text{C}_6\text{H}_4(\text{NH}_2)_2$; acn = Acetonitrile, CH_3CN) has a direct bandgap of 2.67 eV (0.4 eV greater than PbI_2), meaning that the organic cation leads to a blue shift of the bandgap with respect to PbI_2 ; [135] the single layered perovskites $(\text{BDA})\text{PbI}_4$ and $(\text{PEIM})\text{PbI}_3$ have a direct bandgap of 2.64 and 2.73 eV, respectively.[75]

The bandgap type can be determined from Tauc plots.[173] As shown in Figure 8b and 8c, Xiao *et al.* found the $(\text{MA})_2\text{Pb}(\text{SCN})_2\text{I}_2$ material to be an indirect bandgap semiconductor with an indirect bandgap of 2.04 eV and direct bandgap of 2.11 eV.[142] However, Bunsho Ohtani also pointed out that Tauc plots are often mistakenly used to predict the transition mode.[174] The author stated that both direct and indirect Tauc plots had linear parts and it was difficult to determine the mode of transition by comparison of the plots. In this case, first-principles electronic structure calculations serve as effective tools to reveal the nature of the bandgap type.

Fig. 8: (a) Absorbance (A) spectrum of a $(\text{MA})_2\text{Pb}(\text{SCN})_2\text{I}_2$ thin film. (b,c) Tauc plots of the A spectrum corresponding to (b) a direct and (c) an indirect optical bandgap of $(\text{MA})_2\text{Pb}(\text{SCN})_2\text{I}_2$. (d) Diffuse reflectance (R_∞) spectrum of $(\text{MA})_2\text{Pb}(\text{SCN})_2\text{I}_2$ powders. (e,f) Tauc plots of the R_∞ spectrum corresponding to (e) a direct and (f) an indirect optical bandgap of $(\text{MA})_2\text{Pb}(\text{SCN})_2\text{I}_2$. Reproduced and adapted with permission from Ref [142]. Copyright 2016 American Chemical Society.

Fig. 9: Structural and electronic properties of orthorhombic $(\text{MA})_2 \text{Pb}(\text{SCN})_2 \text{I}_2$. (a) Crystal structure viewed along the $[001]$ direction, (b) first Brillouin zone and the k -path used to calculate electronic band structure, (c) calculated electronic band structure and (d) density of states with the HSE $\alpha=43\%$ +SOC method. Reproduced and adapted with permission from Ref [142]. Copyright 2016 American Chemical Society.

B. Mobility Anisotropy

The behavior of charge carriers in semiconducting materials plays an important role in the functionality of optoelectronic devices. To ensure efficient charge transfer, the charge carriers should have high mobility, long lifetimes, and low effective masses. One important character of 2DHPs is the conductivity anisotropy similar to that of two-dimensional electron gases in semiconductor heterostructures.[175] This characteristic means that the charge carriers are highly mobile parallel to the inorganic layers, but immobile in the perpendicular direction across the insulating organic layers.[50, 58, 60, 142] In the side of theoretical and computational studies, the conductivity anisotropy is often indicated by the electron and hole effective masses from the first-principles electronic structure calculations. As proof of concept, our prior work on $(\text{BA})_2 (\text{MA})_{n-1} \text{Pb}_n \text{I}_{3n+1}$ shows small charge carrier effective masses within the 2D plane but extremely large effective masses in the out-of-plane direction, implying a strong mobility anisotropy.[130] Similar phenomena also occur in other 2DHPs, such as $(\text{BA})_2 \text{Pb}_n \text{I}_{3n+1}$, [58] $(\text{MA})_2 \text{Pb}(\text{SCN})_2 \text{I}_2$, [50] and $(\text{MA})_2 \text{CuCl}_x \text{Br}_{4-x}$. [60] Figure 9 shows crystal structure, Brillouin zone, electronic band structure, and DOS of the 2DHP $(\text{MA})_2 \text{Pb}(\text{SCN})_2 \text{I}_2$. [142] The flat bottom conduction band and top valence band along the k -path T-R and Γ -X suggest that the calculated effective masses for holes and electrons approach infinity, and these two reciprocal paths correspond to the a direction of the crystal structure in the real space, see Figure 9a-c. This implies that the charge carriers do not travel between the inorganic layers and thus are tightly confined to the 2D inorganic plane, indicating a strong mobility anisotropy. The calculated DOS shows that VB mostly consists of I $5p$ and S $3p$ states while the CB mainly consists of Pb $6p$ states, see Figure 9d. Table 6 summarizes the calculated effective masses for several 2DHPs.

Table VI: Summary of calculated effective masses parallel and perpendicular to 2D layer planes in units of the free electron rest mass, m_0 . \parallel and \perp indicate the reciprocal lattice vectors parallel and perpendicular to the 2D plane, respectively.

Compound	Type	\parallel	\perp	Ref
$(\text{BA})_2 \text{PbI}_4$	e^-	0.082	∞	[58]
$(\text{BA})_2 (\text{MA})_2 \text{PbI}_4$	e^-	0.097	∞	[58]
$(\text{BA})_2 (\text{MA})_3 \text{PbI}_4$	e^-	0.094	∞	[58]
$(\text{BA})_2 \text{PbI}_4$	h^+	0.144	∞	[58]
$(\text{BA})_2 (\text{MA})_2 \text{PbI}_4$	h^+	0.141	∞	[58]

$(\text{BA})_2 (\text{MA})_3 \text{Pb}$ 4I_{13}	h^+	0.153		∞	[58]
$(\text{MA})_2 \text{CuCl}_4$	e^-	0.31		0.58	[60]
$(\text{MA})_2 \text{CuCl}_2 \text{Br}$ 2	e^-	0.51		1.86	[60]
$(\text{MA})_2 \text{CuClBr}_3$	e^-	0.57		2.39	[60]
$(\text{MA})_2 \text{CuCl}_{0.5}$ $\text{Br}_{3.5}$	e^-	0.52		4.04	[60]
$(\text{MA})_2 \text{CuCl}_4$	h^+	1.71		∞	[60]
$(\text{MA})_2 \text{CuCl}_2 \text{Br}$ 2	h^+	2.67		∞	[60]
$(\text{MA})_2 \text{CuClBr}_3$	h^+	1.51		∞	[60]
$(\text{MA})_2 \text{CuCl}_{0.5}$ $\text{Br}_{3.5}$	h^+	1.55		∞	[60]
$(\text{PEA})_2 \text{PbI}_4$	e^-	0.278			[160]
$(\text{PEA})_2 (\text{MA})\text{Pb}$ 2I_7	e^-	0.198			[160]
$(\text{PEA})_2 (\text{MA})_2$ $\text{Pb}_3 \text{I}_{10}$	e^-	0.214			[160]
$(\text{PEA})_2 \text{PbI}_4$	h^+	0.604			[160]
$(\text{PEA})_2 (\text{MA})\text{Pb}$ 2I_7	h^+	0.391			[160]
$(\text{PEA})_2 (\text{MA})_2$ $\text{Pb}_3 \text{I}_{10}$	h^+	0.232			[160]
$(\text{MA})_2 \text{Pb}(\text{SCN})$ 2I_2	VBM	0.2			[50]
$(\text{MA})_2 \text{Pb}(\text{SCN})$ 2I_2	CBM	0.14			[50]
		T-Z	T-Y		
		[010]	[001]		
$(\text{MA})_2 \text{Pb}(\text{SCN})$ 2I_2	e^-	0.88	0.34	∞	[142]
$(\text{MA})_2 \text{Pb}(\text{SCN})$ 2I_2	e^-	0.37	0.58	∞	[132]

$(\text{MA})_2 \text{Pb}(\text{SCN})_2 \text{I}_2$	e^- (SOC)	0.17	0.2	∞	[132]
$(\text{MA})_2 \text{Pb}(\text{SCN})_2 \text{I}_2$	h^+	0.99	2.36	∞	[142]
$(\text{MA})_2 \text{Pb}(\text{SCN})_2 \text{I}_2$	h^+	1.61	1.43	∞	[132]
$(\text{MA})_2 \text{Pb}(\text{SCN})_2 \text{I}_2$	h^+ (SOC)	0.36	0.45	∞	[132]
$(\text{BA})_2 \text{GeI}_4$	e^-	0.19	0.18		[130]
$(\text{BA})_2 (\text{MA})\text{Ge}_2 \text{I}_7$	e^-	0.23	0.14		[130]
$(\text{BA})_2 (\text{MA})_2 \text{Ge}_3 \text{I}_{10}$	e^-	0.22	0.13		[130]
$(\text{MA})\text{GeI}_3$	e^-	0.22	0.20		[130]
$(\text{BA})_2 \text{GeI}_4$	h^+	0.28	0.27		[130]
$(\text{BA})_2 (\text{MA})\text{Ge}_2 \text{I}_7$	h^+	0.34	0.31		[130]
$(\text{BA})_2 (\text{MA})_2 \text{Ge}_3 \text{I}_{10}$	h^+	0.27	0.26		[130]
$(\text{MA})\text{GeI}_3$	h^+	0.28	0.31		[130]

Table VII: Summary of experimental absorption coefficients (α) of 2DHPs at measured wavelength (l).

Compound	α (mm^{-1})	l (nm)	Ref
$(\text{MA})_2 \text{CuCl}_4$	3500	650	[60]
$(\text{HIA})\text{SnI}_4$	9.444	–	[80]
$(\text{HIA})\text{PbI}_4$	18.175	–	[80]
$(\text{BZA})_2 \text{SnI}_4$	6.575	–	[80]
$(\text{BZA})_2 \text{PbI}_4$	12.76	–	[80]
$(\text{PEA})_2 \text{PbI}_4$	190	800	[176]
$(\text{BA})_2 (\text{MA})\text{Pb}_2 \text{I}_7$	17.712	–	[58]
$(\text{BA})_2 (\text{MA})_2 \text{Pb}_3 \text{I}_{10}$	19.739	–	[58]
$(\text{BA})_2 (\text{MA})_3 \text{Pb}_4 \text{I}_{13}$	21.026	–	[58]
$(\text{BA})_2 (\text{MA})_4 \text{Pb}_5 \text{I}_{16}$	21.777	–	[70]

$(\text{BA})_2(\text{MA})_2\text{Sn}_3\text{I}_{10}$	10000	550	[38]
--	-------	-----	------

C. Light Absorption

Light absorption heavily depends on the electronic properties of the semiconductors including the bandgaps, bandgap type, and charge carrier mobility, as discussed above. It occurs when electrons absorb photons and gain energy to jump higher energy levels, leading to optoelectronic applications such as solar cells and photodetectors, as discussed later. One important parameter to characterize optical absorption properties is the absorption coefficient. It determines the depth into a material that the photons at a particular wavelength can penetrate before they are absorbed. Table VII summarizes the experimental absorption coefficients of several 2DHPs at measured wavelength (if available). A systemic comparison of the light absorption for $(\text{BA})_2(\text{MA})_n\text{Pb}_n\text{I}_{3n+1}$ ($n = 3, 4, \text{ and } 5$) shows that the measured absorption coefficients increase as the film thickness of 2DHPs increases at the same conditions (wavelength and temperature).[58]

The 2DHPs also show multiphoton absorption (MPA) properties for potential technological applications due to the enhanced quantum and dielectric confinement effects.[108, 176] In 2017, Liu *et al.* reported a giant two-photon absorption (TPA) in the 2DHP, $(\text{PEA})_2\text{PbI}_4$, with the TPA coefficient about 211.5 cm MW^{-1} , about one order of magnitude larger than those of 3DHPs.[176] Interestingly, in 2020, Li *et al.* reported a high-order MPA, *i.e.*, 5PA, in the 2DHP, $(\text{IA})_2(\text{MA})_2\text{Pb}_3\text{Br}_{10}$, with a cross section (σ_5) value of $1.2 \times 10^{-132} \text{ cm}^{10} \text{ s}^4 \text{ photon}^{-4}$ (at 2400 nm).[108] The surprising 5PA effect is attributed to the quantum-confined motif of inorganic wells and organic cations that server as barriers, which provides opportunities for next-generation biophotonic applications.

D. Light Emission

Light emission of semiconductors has important technological applications such as large-area display, indicator lights, and energy-efficient light sources. The organic-inorganic hybrid perovskites offer a high color purity regardless of crystal size because of their multiple quantum well structure.[177, 178] In particular, the 2DHPs are promising alternative light-emitters to organic light-emitting diodes and inorganic quantum dot LEDs because of their bandgap tunability and low-temperature solution processability.[37, 38, 51, 55, 58, 87, 119, 142, 147, 159]

2DHPs have been found to emit radiation across the entire visible spectrum upon UV excitation, generating white light.[51, 58, 87, 100, 112] This phenomenon is known as broadband emission, with potential use of layered hybrid perovskites as single-source white-light phosphors. The first instance of broadband emission in layered hybrid perovskites was observed in 2014 by Dohner *et al.* in $(\text{EDBE})\text{PbX}_4$ ($X = \text{Cl, Br, and I}$), $(\text{MPDA})\text{PbBr}_4$, and $(\text{MEDA})\text{PbBr}_4$. [100, 112] Soon after, more efforts were made to explore relationship between the broadband emission and structural distortion of 2DHPs. For example, in 2017, Neogi *et al.* reported a broadband white-light emission in $(\text{CBMA})\text{PbBr}_4$, and attributed this broad emission to self-trapped states that are favored by deformations of the inorganic layers.[91] Mao *et al.* investigated three 2DHPs, α -(DMEN) PbBr_4 , (DMAPA) PbBr_4 , and (DMABA) PbBr_4 , and found that the photoluminescence (PL) emission becomes broadened as the degree of distortion of the inorganic

layers increases, with the most distorted structure having the broadest emission and longest lifetime.[95] Cortecchia *et al.* compared the highly distorted perovskite (EDBE)PbI₄ with the less distorted perovskite (BA)₂PbI₄ and found that only (EDBE)PbI₄ can form lead vacancies that lead to the formation of I₃⁻ and thus a broadened PL, implying an important role of structural distortion in the broadband emission.[161] García-Fernández *et al.* also showed that (DMA)₇Pb₄X₁₅ exhibits a broadband PL related to the structural distortions of the inorganic octahedra.[94]

The defect states and related self-trapped states were proposed to be responsible for the broadband PL emission. Yangui *et al.* studied the relationship between inorganic layer distortion and broadband PL emission in (CHA)₂PbBr₄ and (CHA)₂CdBr₄, and explained this phenomenon from the perspective of self-trapped states.[86, 85] Similarly, Hu *et al.* explored the mechanism of broadband white-light emission in the (110) 2DHP (N-MEDA)[PbBr₄] (N-MEDA = N¹-methylethane-1,2-diammonium) using a suite of ultrafast spectroscopic probes and concluded that the broadband emission is associated with a distribution of local minima in the excited-state potential energy surface with additional contributions from material defects and correlated self-trapped sites from ultrafast spectroscopic measurement.[133] In contrast, Dohner *et al.* studied the PL emission in (EDBE)PbX₄ (X = Cl, Br, and I) and concluded that the emission originates from the bulk material rather than surface defect sites, along with contributions from strong electron-phonon coupling in a deformable lattice, with an inhomogeneous broadening due to a distribution of intrinsic trap states.[100]

The PL spectra can be tuned through multiple factors such as temperature, compositions, and the lattice size.[49, 59, 72, 85, 86, 107, 112] For example, PL spectra could vary with temperature due to phase transitions and changes in the interlayer spacing, with a peak emission at 90K, and the coexistence of white-light emission and excitonic edge emission at lower temperatures.[85, 86] Booker *et al.* reported a red-shifted and broadband emission below 200 K in addition to excitonic photoluminescence in (HA)₂PbI₄ and (DA)₂PbI₄. [107] In contrast, Mitzi *et al.* observed a blue-shift in the emission peak from (BA)₂GeI₄ (690 nm) to (BA)₂SnI₄ (625 nm) to (BA)₂PbI₄ (525 nm) with a progressive increase in the peak sharpness.[72] Dou *et al.* found a PL emission peak at 411 nm in the bulk crystal of (BA)₂PbBr₄ and a slightly shifted peak at 406 nm in its 2D sheets, and verified that this shift is caused by lattice expansions in the 2D sheets from DFT calculations.[59] Soe *et al.* showed that the PL of (GA)(MA)_nPb_nI_{3n+1} increased as they increased the dimensionality of the material.[49] The reduced grain size of the quasi-2DHPs was also proposed for the increased PL emission in the 2D (TFA)₂(MA)_{n-1}Pb_nBr_{3n+1} as compared to that in the 3DHPs.[128] These works suggest a possibility of tuning PL emission via changing the structural parameters of 2DHPs such as lattice size, dimensionality, and grain size.

Fig. 10: Schematic representation of crystal structure, electronic band structure, and photoluminescent properties of quasi-2D perovskites. (a) Crystal structures of (H₃NH₃)₂(MA)_{n-1}Pb_nI_{3n+1} perovskites with n = 1, 3, 5, 10, and ∞, showing the dimensional evolution from 2D to 3D. (b) Band alignment of the 2D perovskite at different <n> values with respect to ITO, TiO₂

, F8, MoO₃, and the Au electrode. (c) The photoluminescence quantum yield of the 2D perovskites with different <n> values at a low excitation intensity (6 mW cm⁻²). (d) Evolution of the photoluminescence quantum yield as a function of the excitation power density at different <n> values. Reproduced and adapted with permission from Ref [53]. Copyright 2016 Springer Nature.

E. Excitonic Properties

Excitonic properties significantly influence the light-emission efficiency of electroluminescent materials, which involve the exciton formation and diffusion, binding energy, and thermal quenching.[179–184] A high exciton binding energy strengthens the stability of excitons against thermal dissociation, allowing for potential applications in room temperature LED devices.

Compared to the 3DHPs, 2DHPs have a much higher exciton binding energy due to sharp dielectric contrast between the high and low dielectric constants of the inorganic and organic layers respectively.[87, 148] The high frequency limit (ϵ_∞)—the dielectric constant—decreases with decreasing layer thickness, but its value is not affected by the size of aliphatic chains.[185] For example, exciton binding energies of (BA)₂(MA)_{n-1}Pb_nI_{3n+1} range from an average value of 220 meV to 270 meV and 380 meV for $n > 2$, $n = 2$ and $n = 1$, respectively, approximately one order of magnitude greater than in 3D lead halide perovskites.[159] In 2015, Yangui *et al.* reported a large exciton binding energy (356 meV) in the 2DHP, (CHA)₂PbI₄, and attributed it to the large dielectric contrast between organic and inorganic layers.[87] The large exciton binding energy was also reported in several other 2DHPs, such as (CHA)₂CdBr₄ (377 meV with a sharp excitonic peak at 3.24 eV),[85] (BA)₂PbI₄ (490 meV),[138] and (CBMA)PbBr₄ (340 meV).[91]

The exciton binding energy of 2DHPs was also studied from first-principles computational study. Our previous calculations on (BA)₂(MA)_{n-1}Ge_nI_{3n+1} shows that its exciton binding energies range from 202 meV to 190 meV, 150 meV, and 34 meV for $n = 1, 2, 3$, and ∞ respectively.[130] Tsai *et al.* calculated the exciton binding energy of (BA)₂(MA)_{n-1}Pb_nI_{3n+1} at $n = 3$ and 4 to be close to that of (MA)₂PbI₃, in agreement with the absence of excitonic signatures in their optical absorption spectra.[39] This suggests that the excitons in (BA)₂(MA)_{n-1}Pb_nI_{3n+1} at $n = 3$ and 4 are nearly ionized at room-temperature, leading to free carrier-dominated charge transport. Soe *et al.* demonstrated that in the ACI perovskite, (GA)(MA)_nPb_nI_{3n+1}, the exciton binding energy is reduced compared to the RP perovskites, and attributed it to the reduced dielectric contrast difference between the inorganic layers and the spacer cations caused by shorter interlayer spacing.[49]

Another unique excitonic property of 2DHPs is the triplet exciton state. A triplet exciton state is a bound electron-hole pair that has a total spin angular momentum of 1, allowing for three values of spin component m_s (-1, 0, 1). These triplet exciton states constitute 75% of excitons that are generated during charge injection. Harnessing these triplet excitons in phosphorescent molecules enables the potential of attaining 100% internal quantum efficiency in phosphor-doped LEDs.[186, 187] The triplet exciton properties of 2DHPs demonstrate their potential applications in the thin film triplet photosensitizers, such as desulfurization of light oil,[188] photooxidation,[189] and photodynamic therapy.[190] For example, Younts *et al.* demonstrated

an efficient generation of triplet exciton states in the thin films of 2DHP, $(\text{MA})_2\text{Pb}(\text{SCN})_2\text{I}_2$, with a corresponding PLQE of 11.7% at 160K and extremely long diffusion lengths of about 152 nm for the generated triplet excitons, which allows an efficient transport across the entire thin film.[151]

Other excitonic properties such as excitonic bandgap, excitonic peak, and exciton-phonon scattering are reviewed here. The exciton band of $(\text{PEA})_2(\text{MA})_2\text{Pb}_3\text{I}_{10}$ ($n = 3$) was found to be 2.06 eV,[54] close to the ideal value (1.9 eV) for the higher band-gap absorber in a dual-absorber tandem device,[191] which can surpass the Shockley-Queisser limit.[192] Abdel-Baki *et al.* measured an excitonic peak at 2.397 eV in $(\text{PEA})_2(\text{MA})\text{PbI}_4$, and found that the exciton relaxation fits to a bi-exponential decay with a free exciton lifetime of about 100 ps and intraband lifetime of < 140 fs.[148] They suggested that the excitons are delocalized in $(\text{PEA})_2(\text{MA})\text{PbI}_4$ ($n = 1$), pointing to the importance of the organic layer in the optoelectronic properties of 2DHPs.

In the Sn-based RP-type 2DHP, $(\text{BA})_2(\text{MA})_{n-1}\text{Sn}_n\text{I}_{3n+1}$, excitonic peaks were found only in the single-layered compounds, suggesting a lower exciton binding energy due to higher dielectric constants.[38] The excitonic bandgap also depends on the organic molecule besides the crystal structure.[116] Guo *et al.* investigated the intrinsic exciton relaxation pathways in the layered $(\text{BA})_2(\text{MA})_{n-1}\text{Pb}_n\text{I}_{3n+1}$ ($n = 1, 2, \text{ and } 3$) structures from time-resolved and temperature-dependent PL studies.[139] They found that the PL decay rate increases with temperature, implying an exciton-phonon scattering. These results also indicate that scattering via deformation potential by acoustic and homopolar phonons is the main scattering mechanism, suggesting that exciton decay is protected from scattering by charge defects and polar optical phonons, thus leading to the efficient screening of Coulomb potential as in 3D perovskites.

The excitonic properties can be tuned by modifying the number of inorganic layers, halide composition, or large organic cation selection. DFT calculations verified that the high frequency limit (ϵ_∞), or the dielectric constant, decreases with decreasing layer thickness, but its value is not affected by the size of aliphatic chains.[185] Niu *et al.* found that exciton amplitude scales linearly with increasing number of layers due to the disorder that causes an inhomogeneous broadening of the exciton resonance.[61] The exciton absorption peaks also show a parabolic relationship with increasing composition of larger halide anions, reaching a maximum at a 50-50 composition of large and small anions.[119] Excitonic properties and the coupling of exciton dynamics with lattice distortions and motion in 2DHPs can also be found in a recent review article.[193]

Fig. 11: DFT studies of defects in 2D perovskite $\text{Rb}_2\text{Pb}_2\text{I}_4$. **a**, Electronic levels of point defects, in which long and short bars denote two degenerate states and a single state, respectively. The blue and red colors indicate spin polarized states; and the occupied states are marked by arrows. **b,c**, Formation energies of point defects (**b**) and line defects (**c**) as a function of I chemical potential along phase boundaries. Reproduced and adapted with permission from Ref [194]. Copyright 2016 American Chemical Society.

F. Defect States

Defect states refer to introduced energy states in the bandgap of a semiconductor by defects such as impurities, vacancies, and self-interstitial atoms. Defects can significantly influence the electronic and optical properties of a semiconductor, including the charge carrier

recombination rate, charge transport, and light absorption and emitting.[195, 196, 197] The deep defects states that appear in the middle of the band gap trap free charge carriers and lead to non-radiative recombination, thus slowing down the charge carrier transport. To maximize device performance such as solar cell efficiency, the density of defect (trap) states should be minimized to reduce competing electron-hole recombination channels.[198, 199]

In 2015, Zhu's research team reported a comparison study for the trap states in the 3DHP, MA PbI_3 , and 2DHP, $(\text{BA})_2 \text{Pb}_{n-1} \text{I}_{3n+1}$, and found that the density of excitonic traps increased from the 3DHP to 2DHP and also as the relative surface area increases within the 2DHP family, suggesting that the trap states are localized at crystallite surfaces and interfaces.[147] Interestingly, the team also found that the presence of chloride in the perovskite thin films can significantly reduce the density of excitonic traps, which might be responsible for the high solar cell performance in this case. Zhou *et al.* demonstrated that the incorporation of appropriate FA^+ ions into $(\text{BA})_2 (\text{MA,FA})_3 \text{Pb}_4 \text{I}_{13}$ produces high-quality films, which reduces the undesired defects and thus reduces the density of non-radiative recombination centers.[157] In 2017, Peng *et al.* reported an extremely low self-doping in single crystals of $(\text{PEA})_2 (\text{MA})_{n-1} \text{Pb}_n \text{I}_{3n+1}$ ($n = 1, 2, 3$), over 3 orders of magnitude lower than that of typical 3DHPs.[160] The authors ascribed it to the presence of the large organic cations that suppress the formation of defects during the crystallization process. Similarly, Byun *et al.* also found that a higher proportion of 2D material in $(\text{PEA})_2 (\text{MA})_{n-1} \text{Pb}_n \text{Br}_{3n+1}$ reduces deep traps, thereby reducing non-radiative recombination.[51] These works suggest that doping appropriate ions can be helpful for reducing the density of defects, and future research efforts on the development of systematic guidelines of dopants selection are desired.

Note that defect states, particularly shallow states, can also be beneficial for optoelectronic applications. For example, Blancon *et al.* reported that edge states in the 2DHP, $(\text{BA})_2 (\text{MA})_{n-1} \text{Pb}_n \text{I}_{3n+1}$ ($n > 2$) extended the optical absorption from visible to near infrared and more importantly provided a direct pathway to dissociate excitons into free charge carriers, which substantially improved the performance of optoelectronic devices.[159] The authors attributed these gap states to the materials surfaces (edges) associated with the inorganic octahedra.

Defect properties were also studied from first-principles calculations. For instance, Liu *et al.* studied electron activities of defects the 2D inorganic perovskite $\text{Rb}_2 \text{PbI}_4$, and found that the deep-level defects can be easily formed at a high chemical of potential of iodine (μ_i),[194] as shown in Figure 11. This is significantly different from the case of 3D perovskites in which the deep-level defects are difficult to form and the dominating defects all have shallow states.[200, 201] Accordingly, the defects in the $\text{Rb}_2 \text{PbI}_4$ s can be tuned to be less harmful for optoelectronic applications by adjusting the crystal synthesis conditions to be Pb-rich and I-poor. Booker *et al.* demonstrated that iodide vacancies do not form gap states while interstitial iodide introduce deep gap states around 0.65 eV above the valence band in the 2DHP $(\text{HA})_2 \text{PbI}_4$ and $(\text{DA})_2 \text{PbI}_4$ from first-principles calculations, which corresponds to an electron transition energy around 2.1 eV from the conduction band edge to these localized states, in good agreement with the white emission at 2.0 eV (625 nm).[107]

G. Multiferroic Properties

Ferroelectricity and ferromagnetism refer to the stable and switchable electrical

polarization and magnetization in a material, respectively. If one material exhibits more than one of the primary ferroic properties, *i.e.*, ferromagnetism, ferroelectricity, and ferroelasticity, then it is also called multiferroic material. Multiferroic materials have a wide variety of potential device applications such as being used for spin filters, magnetic sensors, thermal energy harvesting, and solid state cooling due to their unique physical properties. [202–205]

Interestingly, ferromagnetic and/or ferroelectric properties have been also found in the layered organic-inorganic hybrid compounds. For instance, Liao *et al.* reported a high-temperature molecular ferroelectric behavior in $(\text{BZA})_2\text{PbCl}_4$ with a polarization $P_s = 13 \mu\text{C cm}^{-2}$ and a Curie temperature $T_c = 438 \text{ K}$, which is ascribed to the BZA cation and its reorientation.[81] Guo *et al.* demonstrated a P_s value of $3.2 \mu\text{C cm}^{-2}$ in $(\text{CPA})_4\text{AgBiBr}_8$ (CPA = chloropropylammonium),[90] which is attributed to the spontaneous polarization and dynamic ordering of the organic CPA cations and the tilting motion of the heterometal $\text{AgBr}_6/\text{BiBr}_6$ octahedra. In 2019, Li *et al.* reported a ferroelectric 2DHP, $(\text{BA})_2(\text{MA})\text{Pb}_2\text{Br}_7$, which exhibits a P_s of $3.6 \mu\text{C cm}^{-2}$, and found that the photoresponse was sensitive to the polarization direction due to the intrinsic anisotropy of optical absorption.[206] To be specific, the strongest photoresponse was parallel to P_s (along the *c*-axis) with a large dichroism ratio ($I_{ph}^c/I_{ph}^a \approx 2.0$). These findings suggest that the polarization-sensitive ferroelectric 2DHPs may bring novel optoelectronic applications. In a very recent work, Li *et al.* reported a large ferroelectric polarization of $5 \mu\text{C cm}^{-2}$ in $(\text{IA})_2(\text{MA})_2\text{Pb}_3\text{Br}_{10}$ (IA = isoamylammonium), and found that such a large polarization could promote modulation of multiphoton absorption under external electric fields.[108] The enhanced multiphoton absorption properties in the ferroelectric 2DHP provides potential for next-generation biophotonic applications.

A long-range ferromagnetic ordering below 9K has been observed in the layered compounds A_2CuCl_4 (where A = 4-fluoroanilinium and 4-chloroanilinium), which was ascribed to the intralayer ferromagnetic interaction between Cu^{2+} ions.[84] Han *et al.* synthesized the layered perovskite-like $(\text{MA})_2[\text{Fe}^{\text{II}}\text{Cl}_4]$ and studied its structural and magnetic phase transitions.[110] The authors reported a structural phase transition from high-symmetry $I4/mmm$ ($T > 335 \text{ K}$) to the low-symmetry $Pccn$ ($T < 335 \text{ K}$), and found a hidden-canted antiferromagnetic ground state that can be transformed into a canted antiferromagnet with a metamagnetic critical field greater than 200 Oe. The inorganic-organic hybrid $(\text{PEA})_2\text{CuCl}_4$ is a ferromagnetic insulator and its inorganic component consisting of 2D perovskite-like sheets exhibit a long-range ferromagnetic order below 13 K.[207, 208] Arkenbout *et al.* reported that the cooperative distortion of the inorganic octahedra caused by Jahn-Teller distortion introduces an antiferrodistortive arrangement of the octahedra, thus leading to the ferromagnetic interactions.[209]

In particular, a coexistence of ferromagnetic and ferroelectric ordering with an improper ferroelectric order below 340 K and a ferromagnetic order below 13 K has been found in the layered $(\text{PEA})_2\text{CuCl}_4$ compound.[123] The spatial ordering of hydrogen bonds that link PEA cations to the inorganic CuCl_6 octahedra lead to the electric polarization; while the buckling of the corner-linked CuCl_6 octahedra was responsible for the magnetic superexchange.

Fig. 12: Evolution of materials stability as a function of n for the 2DHP, $(\text{PEA})_2(\text{MA})_{n-1}\text{Pb}_n\text{I}_{3n+1}$. Reproduced and adapted with permission from Ref [210]. Copyright 2016 American Chemical Society.

Table VIII: Summary of key parameters of the 2DHP-based solar cells.

Compound	PCE (%)	V_{oc} (V)	J_{sc} (mA/cm^2)	FF (%)	Ref
$(\text{BA})_2(\text{MA})_2\text{Pb}_3\text{I}_{10}$	4.02	0.929	9.43	46	[37]
$(\text{BA})_2(\text{MA})_3\text{Pb}_4\text{I}_{13}$	12.51	1.01	16.76	74.13	[39]
$(\text{BA})_2(\text{MA})_4\text{Pb}_5\text{I}_{16}$	8.71	1	11.44	75.79	[70]
$(\text{BA})_2(\text{MA})_3\text{Sn}_4\text{I}_{13}$	2.53	0.376	8.7	45.7	[38]
$(\text{PEA})_2(\text{MA})_2\text{Pb}_3\text{I}_{10}$	4.73	1.18	6.72	60	[54]
$(\text{PEA})_2(\text{MA})_{49}\text{Pb}_{50}\text{I}_{151}$	8.5	1.46	9.0	65	[52]
$(\text{MA})_2\text{CuCl}_2\text{Br}_2$	0.017	0.256	0.216	32	[60]
$(\text{HOOC}(\text{CH}_2)_4\text{NH}_3)_2\text{PbI}_4/(\text{MA})\text{PbI}_3$	14.6	1.025	18.84	75.5	[69]
$(\text{HA})_2(\text{MA})\text{Pb}_2\text{I}_7$	0.336	0.71	1.33	35.5	[152]
$(\text{HA})_2(\text{FA})\text{Pb}_2\text{I}_7$	1.26	0.733	2.98	57.4	[152]
$(\text{HA})_2(\text{Cs})\text{Pb}_2\text{I}_7$	0.103	0.327	0.682	46.2	[152]
$(\text{IC}_2\text{H}_4\text{NH}_3)_2(\text{MA})_{n-1}\text{Pb}_n\text{I}_{3n+1}$	8	0.893	14.33	63	[153]
$(\text{IC}_2\text{H}_4\text{NH}_3)_2(\text{MA,FA})_{n-1}\text{Pb}_n\text{I}_{3n+1}$	9.03	0.883	14.88	69	[153]
$(\text{HIA})\text{PbI}_4$	1.13	0.91	2.65	46.7	[80]
$(\text{PEA})_2(\text{MA})_{39}\text{Pb}_{40}\text{I}_{121} + 10\% \text{Cs}$	12.6	0.9	24	59	[88]

$(\text{BA})_2 (\text{MA})_{39} \text{Pb}_{40} \text{I}_{121} + 10\% \text{Cs}$	10.2	0.86	21.4	55	[88]
$(\text{CHA})_2 (\text{MA})_{39} \text{Pb}_{40} \text{I}_{121} + 10\% \text{Cs}$	10.6	0.86	21.9	56	[88]
$(\text{PDA})_2 (\text{MA})_3 \text{Pb}_4 \text{I}_{13}$	13.0				[117]
$(3\text{AMP})(\text{MA})_3 \text{Pb}_4 \text{I}_{13}$	7.32	1.06	10.17	67.6	[48]
$(4\text{AMP})(\text{MA})_2 \text{Pb}_3 \text{I}_{10}$	2.02	0.99	3.05	66.4	[48]
$(\text{BA})_2 \text{PbI}_4 / (\text{MA}) \text{PbI}_3$	19.56	1.11	22.49	78	[140]
$(\text{BA})_2 (\text{MA})_{n-1} \text{Pb}_n \text{I}_{3n+1} / (\text{MA}) \text{PbI}_3$	18.85	1.09	22.59	77	[140]
$(\text{BA})_2 (\text{MA})_{0.8} \text{FA}_{0.2} \text{Pb}_4 \text{I}_{13}$	12.81	0.999	18.12	70.79	[157]
$(\text{GA})(\text{MA})_3 \text{Pb}_3 \text{I}_{10}$	7.26	0.974	9.357	80	[49]
$(\text{BA})_2 (\text{MA})_{n-1} \text{Pb}_n \text{I}_{3n+1}$	17.3	1.01	23.66	72.4	[211]
$(\text{PEA})_2 \text{PbI}_4$	19.42	1.117	23.6	73.7	[212]
$(\text{TPM})_2 (\text{MA}) \text{Pb}_2 \text{I}_7$	19.97	1.132	23.5	75.1	[212]
$(\text{FEA})_2 \text{PbI}_4$	22.2	1.096	25.8	78.4	[213]

H. Stability

One of the major challenges preventing 3DHPs from industrial application is the low stability, especially in the presence of ambient water vapor. 2DHPs serve as a promising solution to this challenge.[29, 37–47] For instance, $(\text{BA})_2 (\text{MA})_2 \text{Pb}_3 \text{I}_{10}$, exposed to 40% humidity for 2 months, did not reveal a PbI_2 peak, demonstrating high moisture resistance.[37] For the Sn-based perovskites, unencapsulated MASnI_3 exposed to air degraded to zero in 3 minutes while $(\text{BA})_2 (\text{MA})_3 \text{Sn}_4 \text{I}_{13}$ under similar conditions only gradually degraded after 30 minutes. When encapsulated, $(\text{BA})_2 (\text{MA})_3 \text{Sn}_4 \text{I}_{13}$ was found to retain 90% of its original efficiency after one month.[38] The near-single-crystalline-quality device by Tsai *et al.* placed under 65% humidity yielded similar results, retaining 70% of its original PCE after 94 days while the traditional 3D device falls to < 10% after the same amount of time.[39] The unencapsulated 2D/3D stacking structures by Lin *et al.* exposed to heating at 95 °C for 100 h maintained 96.5% and 88.2%

efficiency for BA and BAI treatments respectively while their control device degraded to 69.6%. [140] Cheng *et al.* also demonstrated a high stability of the lead-free 2DHP, $(\text{PEA})_2 \text{Ge}_{0.5} \text{Sn}_{0.5} \text{I}_4$, in the ambient air condition with 50% relative humidity for 15 h. [122] Iagher *et al.* found that incorporating Cs into $n = 40$ quasi-2D perovskites of $(\text{R})_2 (\text{A})_{n-1} \text{Pb}_n \text{I}_{3n+1}$ ($\text{R} = \text{PEA}, \text{BA}, \text{or CHA}, \text{A} = \text{MA}$ and/or Cs) led to traces of PbI_2 in the XRD spectra that were not present in the pure quasi-2DHP-based devices after exposure to 205 h of 1 sun illumination and 50% humidity. They attributed this lower stability to the mixture of cations of different ionic radii, leading to strains in the perovskite structure. [88]

The 2DHP-based LED devices also show high stability. For example, the LED devices fabricated from $(\text{TFA})_2 (\text{MA})_{n-1} \text{Pb}_n \text{Br}_{3n+1}$ showed no changes after exposure to 2688 h in air, the high stability of which was attributed to the hydrophobicity of F atoms and the formation of intermolecular hydrogen bonds. [128] Vassilakopoulou *et al.* fabricated LED devices using lead-based 2DHPs, and found that these devices continued to show stable light emission after four months via PL and PL excitation spectra even the devices were exposed to air and light in an unheated and humid environment. [116]

In addition, it is worth mentioning that the devices based on the 2D/3D perovskite junctions that combine the high moisture stability of 2DHPs with the high performance characteristics of 3DHPs provide one solution to overcome the instability issues in the 3DHP-based devices. [214–216] As one example, the 2D/3D perovskite junction device composed of $(\text{AVA})_2 \text{PbI}_4 / (\text{MA}) \text{PbI}_3$ showed no loss in performance after $> 10,000$ hours. [69]

The origin of the high material stability of 2DHPs was also addressed from several theoretical studies. [50, 130, 210] One fundamental difference between 2DHPs and 3DHPs is the presence of long organic molecules in the 2DHPs. Accordingly, it is natural to speculate that the long organic molecules and their influence on the adjacent atomic environments are responsible for the improved stability. Quan *et al.* reported that van der Waals interactions between the capping organic molecules are critical for the improved stability of 2DHPs from DFT calculations. [210] Their calculations show that the energy to remove PEAI from the $(\text{PEA})_2 (\text{MA})_{n-1} \text{Pb}_n \text{I}_{3n+1}$ compounds is higher than that for MAI, reducing the desorption rate and thus slowing the film decomposition.

Figure 12 shows the evolution of material stability and formation energy of $(\text{PEA})_2 (\text{MA})_{n-1} \text{Pb}_n \text{I}_{3n+1}$ as a function of n , indicating higher stability at a lower n . In prior work, our research team analyzed the origin of lead-free 2DHP, $(\text{BA})_2 (\text{MA})_{n-1} \text{Ge}_n \text{I}_{3n+1}$ from DFT calculations. [130] The calculated decomposition energies range from 1.13 eV to 0.69 eV to 0.62 eV to 0.23 eV for $n = 1, 2, 3,$ and ∞ respectively. The higher stability of 2DHPs was attributed to the higher decomposition energies than that of 3DHPs and explained the origin from the Bader charge analysis. To be specific, the Ge-I bonds have a stronger bonding strength in the 2DHPs than that in the 3D MAGeI_3 because of more charge transfer from Ge cations to I anions, thus leading to the improved stability. This phenomenon can be further fundamentally attributed to the weaker electropositivity of BA than that of MA, which further influences the chemical environment of its adjacent I anions and the resulting charge transfer from Ge cations to the I anions. These works highlight the importance of theoretical calculations in understanding the properties of 2DHPs.

V. Devices and Applications

The exceptional optoelectronic properties of 2DHPs lead to many applications such as the well-known solar cells, LEDs, photodetectors, laser cooling, and spin-related quantum information devices.[30, 57, 103, 146] In this section, we reviewed several major device applications of 2DHPs and their device performances.

A. Solar Cells

The performance of solar cells can be evaluated from four parameters: i) PCE, ii) open circuit voltage (V_{oc}), iii) short circuit current density (J_{sc}), and iv) fill factor (FF). These four parameters are different measurements of the useful energy output of a solar cell device. An ideal solar cell should demonstrate high values for each of these four parameters. The PCE is the ratio between useful energy output and energy input in percentage. The V_{oc} is the maximum voltage a solar cell will provide at zero current in volts. The J_{sc} is the current across the solar cell in amperes per unit area when the solar cell is short circuited, where the voltage is zero. The FF is the power at the maximum power point (P_m) divided by V_{oc} and the short circuit current (I_{sc}) in percentage as shown below:

$$FF = \frac{P_m}{V_{oc} \times I_{sc}} \quad (1)$$

The 2DHP-based solar cells have been extensively studied recently, though these devices have not yet shown an efficiency comparable to those fabricated from the (MA)PbI₃-based 3DHPs. Table VIII summarizes the device parameters of the recent 2DHP-based solar cells. In 2015, Cao *et al.* reported a 2DHP-based solar cell device that was fabricated using (BA)₂(MA)₂Pb₃I₁₀, with a photogenerated V_{oc} of 929 mV, J_{sc} of 9.43 mA/cm², FF of 46% and a PCE of 4.02% under AM 1.5G solar illumination.[37] By raising the dimensionality by two to yield (BA)₂(MA)₄Pb₅I₁₆, Stoumpos *et al.* achieved an improved PCE of 8.71%, V_{oc} of 1.0 V, J_{sc} of 11.44 mA/cm², and a FF of 75.79%.[70] Tsai *et al.* further improve the performance and the stability of 2DHP-based solar cell by using the perovskite thin film with a near-single-crystalline quality, reaching a peak PCE of 12.51%, V_{oc} of 1.01 V, J_{sc} of 16.76 mA cm⁻², and FF of 74.13%.[39] The superior performance was ascribed to the enhanced charge transport and mobility due to the nearly perfect vertical orientation of the 2D layers relative to the FTO substrate, implying that the material interface between the 2DHP and its contact layer (electron/hole transport layer) plays an important role in improving the PCE.

The 2DHPs with large n values were also fabricated and studied in the solar cell configuration. Note that these 2DHPs with large n values are not true 2D materials in the strict sense, which are generally called quasi-2D materials. For instance, a device composed of the perovskite (PEA)₂(MA) _{$n-1$} Pb _{n} Br _{$3n+1$} ($n = 40, 50, \text{ and } 60$), where the n was determined from the scanning electron microscopy images, demonstrated a PCE of 6.3%, V_{oc} of 1.3 V, J_{sc} of 8.4 mA/cm², and FF of 50%.[52] Interestingly, the performance metrics further increased to a PCE of 8.5%, V_{oc} of 1.46 V, J_{sc} of 9.0 mA/cm², and FF of 65% with the use of a hole transport

material. The performance maximum was attributed to the reduced mobility and transport, where fewer charges accumulate at the contacts, leading to improved charge extraction and reduced recombination. In addition, the V_{oc} and efficiency were found to increase with increasing n value until $n = 40-50$, where the performance began to decrease for larger n values. This indicates that there exists an optimal n value for achieving the maximum device performance. Similarly, Koh *et al.* also reported a relatively high PCE of 9% using the quasi-2DHP, $(IC_2H_4NH_3)_2(MA)_{n-1}Pb_nI_{3n+1}$, and found that the efficiency could be further improved with preferential crystal orientation and with the addition of the FA cation.[153]

To further improve the device performance, the 2D/3D heterostructures were employed for fabricating the solar cells by incorporating 3DHPs such as $(MA)PbI_3$ and $MAPbBr_3$. [69, 140, 211–213] For example, Grancini *et al.* designed a highly stable 2D/3D perovskite junction by combining the 2DHP, $(HOOC(CH_2)_4NH_3)_2PbI_4$, with the 3DHP, $(MA)PbI_3$, and fabricated stable solar cells with 14.6% PCE, V_{oc} of 1.025 V, J_{sc} of 18.84 mA/cm², and FF of 75.5%. [69] Lin *et al.* also reported a solar cell device based on the 2D/3D stacking structure, with a PCE of 19.56%, J_{sc} of 22.49 mA/cm², V_{oc} of 1.11 V, and FF of 0.78. [140] The enhanced efficiency was attributed to the healing of the surface defects during the formation process of 2DHPs. In a very recent work, Liu *et al.* reported a high PCE of 22% in the perovskite solar cells based on 3D/2D architectures, in which the 2DHP, $(FEA)_2PbI_4$, was deposited onto the 3D perovskite films. This device also shows exceptional moisture stability, attributed to the reduced exposure of the 3D perovskite to moisture due to the presence of the 2DHP. [213]

B. LEDs

The performance metrics of LEDs are often evaluated from the internal and external quantum efficiency. The internal quantum efficiency is defined as the ratio between the number of photons emitted by the active region and the number of electrons injected into the device per unit time; and the external quantum efficiency is defined as the ratio between the number of photons emitted into free space and the number of electrons injected into the device per unit time. [217]

The 2DHP-based LEDs show a higher photoluminescence quantum yield (PLQY) and higher quantum efficiency (QE) than those fabricated from 3DHPs. [51, 53, 121, 128] For example, Yuan *et al.* reported high PLQY values of 10.1% and 10.6% in $(PEA)_2(MA)_{n-1}Pb_nI_{3n+1}$ for $n = 3$ and $n = 4$, respectively, in contrast to a nearly negligible PLQY for 3D perovskites at the same excitation intensity. Using this material, they designed an LED device with a record external quantum efficiency of 8.8% with a corresponding radiance of 80 W sr⁻¹ m⁻² operating at near-infrared wavelengths. [53] The PLQY of the 2DHP-based LEDs was also found sensitive to the thickness of the 2DHPs, *i.e.*, the n values in the chemical formula. As proof of concept, figure 10c and d show the PLQY of $(PEA)_2(MA)_{n-1}Pb_nI_{3n+1}$ as a function of number of layers (n) and as a function of excitation power density at different n values, respectively, from which an optimal n value for PLQY can be easily derived. [53] Byun *et al.* also reported that the 2DHP-based LED, fabricated from $(PEA)_2PbBr_4$, has a higher current efficiency and luminance than that fabricated from 3DHP, $(MA)PbBr_3$. [51] Moreover, the device fabricated from a mixture of $(PEA)_2PbBr_4$ and $(MA)PbBr_3$ shows the best performance, with the highest luminescence (2935 cd m⁻²) and current efficiency (4.9 cd A⁻¹) with a QE of 34%, which was attributed to i) fully homogeneous

perovskite films formed with small particle size, low trap density, and decent charge transport property. The $(\text{TFA})_2(\text{MA})_{n-1}\text{Pb}_n\text{Br}_{3n}$ -based LED prepared by Jia *et al.* demonstrated a maximum luminance of $1.2 \times 10^3 \text{ cd/m}^2$ and current efficiency up to 0.4 cd/A , a twenty-fold enhancement compared to that of $(\text{MA})\text{PbBr}_3$. [128] Lanzetta *et al.* found that the QE of thin films of $(\text{PEA})_2\text{SnI}_x\text{Br}_{4-x}$ ranged from 0.24% to 0.04% and decreased as Br concentration increased but remained consistently higher than that of the 3D perovskite, MASnI_3 (QE = 0.01%), [121] suggesting that the QE can be optimized via tuning chemical compositions of 2DHPs. Using this material, they constructed an electroluminescent device that reaches a luminance of 0.15 cd/m^2 at 4.7 mA/cm^2 and an efficacy of 0.029 cd/A at 3.6 V. The QE of $(\text{CBMA})\text{PbBr}_4$ was measured to be 1.5%, [91] and the room-temperature QE of $(\text{FA},\text{GA})\text{PbI}_4$ was found to be 3.5%. [101]

C. Photodetectors

The device performance of photodetectors is mainly evaluated from its sensitivity, which can be measured from three metrics: i) quantum efficiency, ii) responsivity and iii) noise current. As discussed above, the quantum efficiency is also one important performance parameter for LEDs. The responsivity measures the electric current flow per watt of optical input.

Owing to the high carrier mobility and good compatibility with flexible substrates, 2DHPs are also suitable for photodetectors. In 2016, Tan *et al.* reported the first photodetector based on the 2D $(\text{BA})_2\text{PbBr}_4$ using the monolayer graphene as an electric contact and protection layer. The device shows promising performance, such as a high responsivity ($\sim 2100 \text{ A/W}$), low dark current ($\sim 10^{-10} \text{ A}$), and high on/off current ratio ($\sim 10^3$). [218] Soon after, Chen *et al.* fabricated a photodetector using the quasi 2D perovskite, $(\text{BA})_2(\text{MA})_{n-1}\text{Pb}_n\text{Br}_{3n+1}$, and their device achieved a photoresponsivity of 190 mA/W , much higher than that of the MAPbI_3 nanoplatelet photodetector (23.3 mA/W), [219] and an on/off current ratio as high as 2.3×10^3 . [146] The optoelectronic performance is expected to be further enhanced upon optimization of semiconductor-electrode contact. The device parameters of several previously reported 2DHP-based photodetectors were also summarized in a recent article. [47]

Although the 2DHP-based photodetectors hold great promise in the photodetection field, their response speed is relatively low ($\approx \text{ms}$), and hence one possible future research direction is to develop new candidates for superfast photodetection. In a very recent work, Han *et al.* reported photodetectors fabricated on the $(\text{PA})_2(\text{FA})\text{Pb}_2\text{I}_7$ that exhibits a superfast response time up to $\approx 2.54 \text{ ns}$, with a high photodetectivity ($\approx 1.73 \times 10^4 \text{ Jones}$), switching ratios ($> 10^3$), and low dark current ($\approx 10 \text{ pA}$). [220] The superfast response speed might be ascribed to the device configuration, that is, the lateral-type detectors fabricated on the highly oriented thin film of 2DHPs have an orientation parallel to the 2D inorganic perovskite layers. Accordingly, in addition to the optimization of semiconductor-electrode contact, appropriate usage of highly oriented thin films of 2DHPs could also be one major future research direction for developing high-performance photodetectors.

D. Quantum Information

2DHPs also show potential for quantum information applications because of their unique properties. The advantages of 2DHPs in this application field can be summarized as four aspects: i)

strong spin-orbit coupling for spin selectivity, ii) high charge-carrier mobility for electronic integration, iii) room-temperature operation for practical applications, and iv) flexible tunability for tuning light-matter coupling strength. For example, in 2016, Giovanni *et al.* reported a strong room-temperature spin-selective optical Stark effect in the 2DHP, (FPEA)₂PbI₄, (FPEA = fluorophenethylammonium, C₆H₄F(CH₂)₂NH₃⁺), demonstrating new prospects to achieve opto-spin logic for quantum information applications. The authors realized exciton spin states that are selectively tuned by ~ 6.3 meV using circularly polarized optical pulses, much larger than any conventional systems.[103] One of the future research directions can be on the substitution of the organic components for achieving enhanced functionalities.

VI. Summary and Outlook

In summary, this review covered several main themes of current research in the area of 2DHPs, including materials synthesis, characterization, optoelectronic and multiferroic properties, defect states, stability and related devices and applications, along with first-principles computational and theoretical studies. The structure of 2DHPs consists of distorted inorganic layers separated by large organic molecules, which leads to unique anisotropic properties and also improves the moisture stability. 2DHPs offer a promising solution to overcome the issue of moisture stability in the 3DHPs. In spite of this, there is still much space to discover and develop 2DHPs either for further improving their PCEs to allow them to be viable alternatives to 3D perovskite solar cells or for exploring their novel properties for various functional applications. Here we discuss several possible future research directions:

i) Computational modeling is powerful to advance the fundamental understanding of the properties of 2DHPs and to speed up the discovery and development of novel 2DHPs. However, there still exist great computational challenges for this class of materials mainly because of the structural complexity of 2DHPs that involves various types of organic molecules. Therefore, future research efforts on the development of easy-to-use infrastructures for the high-throughput *ab-initio* design of 2DHPs are highly desired, for example, by including a list of commonly used organic molecules, as shown in Table 1 in this article. Such computational and software development efforts will be extremely helpful for high-throughput computational studies of 2DHPs. On the one hand, these results will guide the choice of molecules for high device performance by elucidating the relationships among the structure, phase purity, orientation, quantum well thickness, and materials properties. On the other hand, the developed structure-property relationships can also guide the precise orientation, phase-purity control, and manipulation of the structural distortion of inorganic layers of the 2DHPs to further optimize their properties, such as the conversion of the bandgap type from indirect to direct in certain types of 2D perovskites.

ii) The presence of toxic lead has been a long-term concern for practical applications based on the halide lead perovskites including 2DHPs. In this regard, to search for lead-free 2DHPs with robust materials stability and good device performance requires continuous efforts in the future. In particular, high-throughput computational materials screening approach is expected to play an increasing role.[221–224]

iii) To achieve long-term robust device stability and maintain high device performance, some engineering approaches such as the manipulation of effective combination between inorganic layers and organic linkers and applying strain engineering[27, 225–227] and/or interfacial engineering[228–231] via epitaxial growth of 2DHPs could be further explored.

iv) To achieve optimized materials properties of 2DHPs, besides tuning the chemical compositions of inorganic metal cations, an alternative method is to employ molecular engineering, i.e., incorporation of organic ligands and the utilization of the intramolecular and/or intermolecular interactions in the 2DHPs. As indicated by recent work,[232–236] such a route could lead to enhanced electronic and optical properties and improved stability. For example, Passarelli *et al.* reported an enhanced out-of-plane conductivity and photovoltaic performance in the layered (aromatic-O-linker-NH₃)₂PbI₄. [232] It was attributed to the better HOMO and LUMO alignment between inorganic layers and organic components, caused by the intramolecular hydrogen bonding in the organic cations and supramolecular π bonding interactions. Dou's research team reported that the incorporation of conjugated ligands not only improved the charge injections but also promoted the formation of large grains and stabilized the inorganic layers of the 2DHPs. [233, 234] In addition, the incorporation of chiral organic ligands could serve as one method to achieve strong circularly polarized light (CPL) emission in 2DHPs. For example, Ma *et al.* reported a strong CPL emission and sensitive CPL detection in the chiral (S- and R-MBA)PbI₄ crystals (MBA = methylbenzylamine, C₆H₅C₂H₄NH₃);[235] a circularly polarized light could be obtained in the 2DHPs by incorporating chiral organic components.[236] In short, as a new research area, molecular engineering could offer a large opportunity to design novel 2DHPs with enhanced functionalities.

v) In addition to the extensively studied photovoltaic, light-emitting, and photodetector applications, 2DHPs also show novel potential applications such as the wearable and flexible electronic devices, quantum computing, and quantum information technologies. For example, flexible photoluminescent films have been fabricated via using a mix of 2D and 3D perovskites into porous silica matrices;[237] spin selectivity has been observed in the 2D-layered hybrid lead-iodine perovskites, with a highest spin-polarization transport of up to 86%, suggesting future spintronic applications.[238] In short, novel functional applications beyond photovoltaics and light emission of 2DHPs remain to be explored.

VII. Acknowledgment

This work was supported by Academic Senate General Campus Research Grant Committee at University of California San Diego and National Science Foundation under award number ACI-1550404.

References

- [1] A. Kojima, K. Teshima, Y. Shirai, T. Miyasaka, *J. Am. Chem. Soc.* **2009**, *131* 6050.
- [2] G. Hodes, *Science* **2013**, *342* 317.
- [3] M. Liu, M. B. Johnston, H. J. Snaith, *Nature* **2013**, *501* 395.

- [4] J. Burschka, N. Pellet, S.-J. Moon, R. Humphry-Baker, P. Gao, M. K. Nazeeruddin, M. Grätzel, *Nature* **2013**, 499 316.
- [5] M. Gratzel, *Nat. Mater.* **2014**, 13 838.
- [6] H. Zhou, Q. Chen, G. Li, S. Luo, T.-b. Song, H.-S. Duan, Z. Hong, J. You, Y. Liu, Y. Yang, *Science* **2014**, 345 542.
- [7] F. Hao, C. C. Stoumpos, D. H. Cao, R. P. H. Chang, M. G. Kanatzidis, *Nat. Photon.* **2014**, 8 489.
- [8] C. C. Stoumpos, C. D. Malliakas, M. G. Kanatzidis, *Inorg. Chem.* **2013**, 52 9019.
- [9] N. J. Jeon, J. H. Noh, Y. C. Kim, W. S. Yang, S. Ryu, S. I. Seok, *Nat. Mater.* **2014**, 13 897.
- [10] N. J. Jeon, J. H. Noh, W. S. Yang, Y. C. Kim, S. Ryu, J. Seo, S. I. Seok, *Nature* **2015**, 517 476.
- [11] T. Baikie, Y. Fang, J. M. Kadro, M. Schreyer, F. Wei, S. G. Mhaisalkar, M. Graetzel, T. J. White, *J. Mater. Chem. A* **2013**, 1 5628.
- [12] J.-H. Im, I.-H. Jang, N. Pellet, M. Grätzel, N.-G. Park, *Nat. Nanotechnol.* **2014**, 9 927.
- [13] W. S. Yang, J. H. Noh, N. J. Jeon, Y. C. Kim, S. Ryu, J. Seo, S. I. Seok, *Science* **2015**, 348 1234.
- [14] G. Xing, N. Mathews, S. Sun, S. S. Lim, Y. M. Lam, M. Grätzel, S. Mhaisalkar, T. C. Sum, *Science* **2013**, 342 344.
- [15] S. D. Stranks, G. E. Eperon, G. Grancini, C. Menelaou, M. J. Alcocer, T. Leijtens, L. M. Herz, A. Petrozza, H. J. Snaith, *Science* **2013**, 342 341.

- [16] D. Shi, V. Adinolfi, R. Comin, M. Yuan, E. Alarousu, A. Buin, Y. Chen, S. Hoogland, A. Rothenberger, K. Katsiev, et al., *Science* **2015**, 347 519.
- [17] Q. Dong, Y. Fang, Y. Shao, P. Mulligan, J. Qiu, L. Cao, J. Huang, *Science* **2015**, 347 967.
- [18] H. Zhu, K. Miyata, Y. Fu, J. Wang, P. P. Joshi, D. Niesner, K. W. Williams, S. Jin, X.-Y. Zhu, *Science* **2016**, 353 1409.
- [19] H. Zhu, Y. Fu, F. Meng, X. Wu, Z. Gong, Q. Ding, M. V. Gustafsson, M. T. Trinh, S. Jin, X.-Y. Zhu, *Nat. Mater.* **2015**, 14 636.
- [20] W. S. Yang, B.-W. Park, E. H. Jung, N. J. Jeon, Y. C. Kim, D. U. Lee, S. S. Shin, J. Seo, E. K. Kim, J. H. Noh, S. I. Seok, *Science* **2017**, 356 1376.
- [21] D. W. deQuilettes, S. M. Vorpahl, S. D. Stranks, H. Nagaoka, G. E. Eperon, M. E. Ziffer, H. J. Snaith, D. S. Ginger, *Science* **2015**, 348 683.
- [22] A. Mei, X. Li, L. Liu, Z. Ku, T. Liu, Y. Rong, M. Xu, M. Hu, J. Chen, Y. Yang, M. Grätzel, H. Han, *Science* **2014**, 345 295.
- [23] W. Chen, Y. Wu, Y. Yue, J. Liu, W. Zhang, X. Yang, H. Chen, E. Bi, I. Ashraful, M. Grätzel, L. Han, *Science* **2015**, 350 944.
- [24] D. B. Mitzi, *J. Chem. Soc., Dalton Trans.* **2001**, 1 1.
- [25] K. Miyata, D. Meggiolaro, M. T. Trinh, P. P. Joshi, E. Mosconi, S. C. Jones, F. De Angelis, X.-Y. Zhu, *Sci. Adv.* **2017**, 3 e1701217.
- [26] D. P. McMeekin, G. Sadoughi, W. Rehman, G. E. Eperon, M. Saliba, M. T. Hörantner, A. Haghighirad, N. Sakai, L. Korte, B. Rech, M. B. Johnston, L. M. Herz, H. J. Snaith, *Science* **2016**, 351 151.
- [27] Y. Li, M. Behtash, J. Wong, K. Yang, *J. Phys. Chem. C* **2018**, 122 177.

[28] N. R. E. Laboratory, Research cell record efficiency chart, **2020**, URL <https://www.nrel.gov/pv/assets/images/efficiency-chart.png>, [Online; accessed October, 2020].

[29] G. Niu, X. Guo, L. Wang, *J. Mater. Chem. A* **2015**, 3 8970.

[30] K. Hong, Q. V. Le, S. Y. Kim, H. W. Jang, *J. Mater. Chem. C* **2018**, 6 2189.

[31] T. M. Brenner, D. A. Egger, L. Kronik, G. Hodes, D. Cahen, *Nat. Rev. Mater.* **2016**, 1 15007.

[32] F. Zhang, H. Lu, J. Tong, J. J. Berry, M. C. Beard, K. Zhu, *Energy Environ. Sci.* **2020**, 13, 4 1154.

[33] G. Niu, W. Li, F. Meng, L. Wang, H. Dong, Y. Qiu, *J. Mater. Chem. A* **2014**, 2 705.

[34] Y. Han, S. Meyer, Y. Dkhissi, K. Weber, J. M. Pringle, U. Bach, L. Spiccia, Y.-B. Cheng, *J. Mater. Chem. A* **2015**, 3 8139.

[35] A. Buin, P. Pietsch, J. Xu, O. Voznyy, A. H. Ip, R. Comin, E. H. Sargent, *Nano Lett.* **2014**, 14 6281.

[36] G. P. Nagabhushana, R. Shivaramaiah, A. Navrotsky, *Proc. Natl. Acad. Sci.* **2016**, 113 7717.

[37] D. H. Cao, C. C. Stoumpos, O. K. Farha, J. T. Hupp, M. G. Kanatzidis, *J. Am. Chem. Soc.* **2015**, 137 7843.

[38] D. H. Cao, C. C. Stoumpos, T. Yokoyama, J. L. Logsdon, T.-B. Song, O. K. Farha, M. R. Wasielewski, J. T. Hupp, M. G. Kanatzidis, *ACS Energy Lett.* **2017**, 2 982.

[39] H. Tsai, W. Nie, J.-C. Blancon, C. C. Stoumpos, R. Asadpour, B. Harutyunyan, A. J. Neukirch, R. Verduzco, J. J. Crochet, S. Tretiak, L. Pedesseau, J. Even, M. A. Alam, G. Gupta, J. Lou, P. M. Ajayan, M. J. Bedzyk, M. G. Kanatzidis, A. D. Mohite, *Nature* **2016**, 536 312.

- [40] L. Mao, C. C. Stoumpos, M. G. Kanatzidis, *J. Am. Chem. Soc.* **2019**, *141* 1171.
- [41] C. Ortiz-Cervantes, P. Carmona-Monroy, D. Solis-Ibarra, *ChemSusChem* **2019**, *12*, 8 1560.
- [42] C. Lan, Z. Zhou, R. Wei, J. C. Ho, *Mater. Today Energy* **2019**, *11* 61.
- [43] L. Zhang, Y. Liu, Z. Yang, S. Liu, *J. Energy Chem.* **2019**, *37* 97.
- [44] S. Ahmad, X. Guo, *Chin. Chem. Lett.* **2018**, *29* 657.
- [45] G. Grancini, M. K. Nazeeruddin, *Nature Reviews Materials* **2018**, *4*, 1 4.
- [46] P. Zhu, J. Zhu, *InfoMat* **2020**, *2* 341.
- [47] P. Chen, Y. Bai, M. Lyu, J.-H. Yun, M. Hao, L. Wang, *Sol. RRL* **2018**, *2* 1700186.
- [48] L. Mao, W. Ke, L. Pedesseau, Y. Wu, C. Katan, J. Even, M. R. Wasielewski, C. C. Stoumpos, M. G. Kanatzidis, *J. Am. Chem. Soc.* **2018**, *140* 3775.
- [49] C. M. M. Soe, C. C. Stoumpos, M. Kepenekian, B. Traoré, H. Tsai, W. Nie, B. Wang, C. Katan, R. Seshadri, A. D. Mohite, J. Even, T. J. Marks, M. G. Kanatzidis, *J. Am. Chem. Soc.* **2017**, *139* 16297.
- [50] A. M. Ganose, C. N. Savory, D. O. Scanlon, *J. Phys. Chem. Lett.* **2015**, *6* 4594.
- [51] J. Byun, H. Cho, C. Wolf, M. Jang, A. Sadhanala, R. H. Friend, H. Yang, T.-W. Lee, *Adv. Mater.* **2016**, *28* 7515.
- [52] B.-E. Cohen, M. Wierzbowska, L. Etgar, *Adv. Fun. Mater.* **2016**, *27* 1604733.

[53] M. Yuan, L. N. Quan, R. Comin, G. Walters, R. Sabatini, O. Voznyy, Y. Hoogland, Sjoerdand Zhao, E. M. Beauregard, P. Kanjanaboos, Z. Lu, D. H. Kim, E. H. Sargent, *Nat. Nanotechnol.* **2016**, *11* 872.

[54] I. C. Smith, E. T. Hoke, D. Solis-Ibarra, M. D. McGehee, H. I. Karunadasa, *Angew. Chem.* **2014**, *126* 11414.

[55] S. Zhang, G. Lanty, J.-S. Lauret, E. Deleporte, P. Audebert, L. Galmiche, *Acta Mater.* **2009**, *57* 3301.

[56] S. Ma, M. Cai, T. Cheng, X. Ding, X. Shi, A. Alsaedi, T. Hayat, Y. Ding, Z. Tan, S. Dai, *Sci. China Mater.* **2018**, *61* 1257.

[57] S.-T. Ha, C. Shen, J. Zhang, Q. Xiong, *Nat. Photon.* **2015**, *10* 115.

[58] C. C. Stoumpos, D. H. Cao, D. J. Clark, J. Young, J. M. Rondinelli, J. I. Jang, J. T. Hupp, M. G. Kanatzidis, *Chem. Mater.* **2016**, *28* 2852.

[59] L. Dou, A. B. Wong, Y. Yu, M. Lai, N. Kornienko, S. W. Eaton, A. Fu, C. G. Bischak, J. Ma, T. Ding, N. S. Ginsberg, L.-W. Wang, A. P. Alivisatos, P. Yang, *Science* **2015**, *349* 1518.

[60] D. Cortecchia, H. A. Dewi, J. Yin, A. Bruno, S. Chen, T. Baikie, P. P. Boix, M. Grätzel, S. Mhaisalkar, C. Soci, N. Mathews, *Inorg. Chem.* **2016**, *55* 1044.

[61] W. Niu, A. Eiden, G. V. Prakash, J. J. Baumberg, *Appl. Phys. Lett.* **2014**, *104* 171111.

[62] E. I. Marchenko, S. A. Fateev, A. A. Petrov, V. V. Korolev, A. Mitrofanov, A. V. Petrov, E. A. Goodilin, A. B. Tarasov, *Chem. Mater.* **2020**, *32*, 17 7383.

[63] Y. Takahashi, R. Obara, K. Nakagawa, M. Nakano, J. ya Tokita, T. Inabe, *Chem. Mater.* **2007**, *19*, 25 6312.

[64] D. B. Mitzi, K. Chondroudis, C. R. Kagan, *Inorg. Chem.* **1999**, *38*, 26 6246.

- [65] Y. Li, G. Zheng, J. Lin, *Eur. J. Inorg. Chem.* **2008**, 2008, 10 1689.
- [66] A. H. Proppe, R. Quintero-Bermudez, H. Tan, O. Voznyy, S. O. Kelley, E. H. Sargent, *J. Am. Chem. Soc.* **2018**, 140, 8 2890.
- [67] H. Yu, Z. Wei, Y. Hao, Z. Liang, Z. Fu, H. Cai, *New J. Chem.* **2017**, 41, 18 9586.
- [68] Y. Li, G. Zheng, C. Lin, J. Lin, *Cryst. Growth Des.* **2008**, 8, 6 1990.
- [69] G. Grancini, C. Carmona, I. Zimmermann, E. Mosconi, X. Lee, D. Martineau, S. Narbey, F. Oswald, F. Angelis, M. Graetzel, M. Nazeeruddin, *Nat. Commun.* **2017**, 8 1.
- [70] C. C. Stoumpos, C. M. M. Soe, H. Tsai, W. Nie, J.-C. Blancon, D. H. Cao, F. Liu, B. Traoré, C. Katan, J. Even, A. D. Mohite, M. G. Kanatzidis, *Chem* **2017**, 2 427.
- [71] D. B. Mitzi, C. A. Feild, W. T. A. Harrison, A. M. Guloy, *Nature* **1994**, 369, 6480 467.
- [72] D. B. Mitzi, *Chem. Mater.* **1996**, 8 791.
- [73] X.-H. Zhu, N. Mercier, P. Frère, P. Blanchard, J. Roncali, M. Allain, C. Pasquier, A. Riou, *Inorg. Chem.* **2003**, 42, 17 5330.
- [74] A. Fraccarollo, L. Marchese, M. Cossi, *J. Phys. Chem. C* **2018**, 122 3677.
- [75] K. Xiong, W. Liu, S. J. Teat, L. An, H. Wang, T. J. Emge, J. Li, *J. Solid State Chem.* **2015**, 230 143.
- [76] M. K. Rayner, D. G. Billing, *Acta Crystallogr., Sect. E: Struct. Rep.* **2010**, 66, 6 m660.
- [77] H. Pan, X. Zhao, X. Gong, Y. Shen, M. Wang, *J. Phys. Chem. Lett.* **2019**, 10, 8

1813.

- [78] D. Solis-Ibarra, H. I. Karunadasa, *Angew. Chem. Int. Ed.* **2013**, *53*, 4 1039.
- [79] C. Lermer, S. P. Harm, S. T. Birkhold, J. A. Jaser, C. M. Kutz, P. Mayer, L. Schmidt-Mende, B. V. Lotsch, *Z. Anorg. Allg. Chem.* **2016**, *642*, 23 1369.
- [80] L. Mao, H. Tsai, W. Nie, L. Ma, J. Im, C. C. Stoumpos, C. D. Malliakas, F. Hao, M. R. Wasielewski, A. D. Mohite, M. G. Kanatzidis, *Chem. Mater.* **2016**, *28* 7781.
- [81] W.-Q. Liao, Y. Zhang, C.-L. Hu, J.-G. Mao, H.-Y. Ye, P.-F. Li, S. D. Huang, R.-G. Xiong, *Nat. Commun.* **2015**, *6* 7338.
- [82] A. B. Corradi, A. M. Ferrari, L. Righi, P. Sgarabotto, *Inorg. Chem.* **2001**, *40*, 2 218.
- [83] K. Pradeesh, K. N. Rao, G. V. Prakash, *J. Appl. Phys.* **2013**, *113* 083523.
- [84] A. K. Vishwakarma, P. S. Ghalsasi, A. Navamoney, Y. Lan, A. Powell, *Polyhedron* **2011**, *30* 1565.
- [85] A. Yangui, S. Pillet, E.-E. Bendeif, A. Lusson, S. Triki, Y. Abid, K. Boukheddaden, *ACS Photonics* **2018**, *5* 1599.
- [86] A. Yangui, D. Garrot, J. S. Lauret, A. Lusson, G. Bouchez, E. Deleporte, S. Pillet, E. Bendeif, M. Castro, S. Triki, Y. Abid, K. Boukheddaden, *J. Phys. Chem. C* **2015**, *119* 23638.
- [87] A. Yangui, S. Pillet, A. Mlayah, A. Lusson, G. Bouchez, S. Triki, Y. Abid, K. Boukheddaden, *J. Chem. Phys.* **2015**, *143* 224201.
- [88] L. Iagher, L. Etgar, *ACS Energy Lett.* **2018**, *3* 366.
- [89] S. Zhang, P. Audebert, Y. Wei, J.-S. Lauret, L. Galmiche, E. Deleporte, *J. Mater. Chem.* **2011**, *21*, 2 466.

- [90] W. Guo, X. Liu, S. Han, Y. Liu, Z. Xu, M. Hong, J. Luo, Z. Sun, *Angew. Chem.* **2020**, *132* 13983.
- [91] I. Neogi, A. Bruno, D. Bahulayan, T. W. Goh, B. Ghosh, R. Ganguly, D. Cortecchia, T. C. Sum, C. Soci, N. Mathews, S. G. Mhaisalkar, *ChemSusChem* **2017**, *10* 3765.
- [92] K. Pradeesh, G. S. Yadav, M. Singh, G. V. Prakash, *Mater. Chem. Phys* **2010**, *124*, 1 44.
- [93] A. Lemmerer, D. G. Billing, *CrystEngComm* **2012**, *14*, 6 1954.
- [94] A. García-Fernández, J. M. Bermúdez-García, S. Castro-García, A. L. Llamas-Saiz, R. Artiaga, J. J. López-Beceiro, M. Sánchez-Andujar, M. A. Señarís-Rodríguez, *Inorg. Chem.* **2018**, *57* 3215.
- [95] L. Mao, Y. Wu, C. C. Stoumpos, M. R. Wasielewski, M. G. Kanatzidis, *J. Am. Chem. Soc.* **2017**, *139* 5210.
- [96] A. Lemmerer, D. G. Billing, *CrystEngComm* **2010**, *12* 1290.
- [97] M. Geselle, H. Fuess, *New Cryst. Struct.* **1997**, *212*, 1 241.
- [98] L. Mao, Y. Wu, C. C. Stoumpos, B. Traore, C. Katan, J. Even, M. R. Wasielewski, M. G. Kanatzidis, *J. Am. Chem. Soc.* **2017**, *139*, 34 11956.
- [99] A. Fraccarollo, V. Cantatore, G. Boschetto, L. Marchese, M. Cossi, *J. Chem. Phys.* **2016**, *144* 164701.
- [100] E. R. Dohner, A. Jaffe, L. R. Bradshaw, H. I. Karunadasa, *J. Am. Chem. Soc.* **2014**, *136* 13154.
- [101] O. Nazarenko, M. R. Kotyrba, S. Yakunin, M. Aebli, G. Rainó, B. M. Benin, M. Wörle, M. V. Kovalenko, *J. Am. Chem. Soc.* **2018**, *140* 3850.

- [102] D. B. Mitzi, C. D. Dimitrakopoulos, L. L. Kosbar, *Chem. Mater.* **2001**, *13*, 10 3728.
- [103] D. Giovanni, W. K. Chong, H. A. Dewi, K. Thirumal, I. Neogi, R. Ramesh, S. Mhaisalkar, N. Mathews, T. C. Sum, *Sci. Adv.* **2016**, *2* e1600477.
- [104] J. Hu, I. W. H. Oswald, H. Hu, S. J. Stuard, M. M. Nahid, L. Yan, Z. Chen, H. Ade, J. R. Neilson, W. You, *ACS Materials Lett.* **2019**, *1*, 1 171.
- [105] I.-H. Park, L. Chu, K. Leng, Y. F. Choy, W. Liu, I. Abdelwahab, Z. Zhu, Z. Ma, W. Chen, Q.-H. Xu, G. Eda, K. P. Loh, *Adv. Fun. Mater.* **2019**, *29*, 39 1904810.
- [106] W. Paritmongkol, N. S. Dahod, A. Stollmann, N. Mao, C. Settens, S.-L. Zheng, W. A. Tisdale, *Chem. Mater.* **2019**, *31*, 15 5592.
- [107] E. P. Booker, T. H. Thomas, C. Quarti, M. R. Stanton, C. D. Dashwood, A. J. Gillett, J. M. Richter, A. J. Pearson, N. J. L. K. Davis, H. Siringhaus, M. B. Price, N. C. Greenham, D. Beljonne, S. E. Dutton, F. Deschler, *J. Am. Chem. Soc.* **2017**, *139* 18632.
- [108] M. Li, Y. Xu, S. Han, J. Xu, Z. Xie, Y. Liu, Z. Xu, M. Hong, J. Luo, Z. Sun, *Adv. Mater.* **2020**, *32* 2002972.
- [109] T. Nakajima, H. Yamauchi, T. Goto, M. Yoshizawa, T. Suzuki, T. Fujimura, *J. Magn. Mater.* **1983**, *31-34* 1189.
- [110] J. Han, S. Nishihara, K. Inoue, M. Kurmoo, *Inorg. Chem.* **2014**, *53* 2068.
- [111] M. Daub, H. Hillebrecht, *Angew. Chem. Int. Ed.* **2015**, *54* 11016.
- [112] E. R. Dohner, E. T. Hoke, H. I. Karunadasa, *J. Am. Chem. Soc.* **2014**, *136* 1718.
- [113] A. B. Corradi, A. M. Ferrari, G. C. Pellacani, A. Sacconi, F. Sandrolini, P. Sgarabotto, *Inorg. Chem.* **1999**, *38*, 4 716.

[114] H. Ren, S. Yu, L. Chao, Y. Xia, Y. Sun, S. Zuo, F. Li, T. Niu, Y. Yang, H. Ju, B. Li, H. Du, X. Gao, J. Zhang, J. Wang, L. Zhang, Y. Chen, W. Huang, *Nat. Photon.* **2020**, *14*, 3 154.

[115] K. zhao Du, Q. Tu, X. Zhang, Q. Han, J. Liu, S. Zauscher, D. B. Mitzi, *Inorg. Chem.* **2017**, *56*, 15 9291.

[116] A. Vassilakopoulou, D. Papadatos, I. Zakouras, I. Koutselas, *J. Alloys Compound.* **2017**, 692 589.

[117] C. Ma, D. Shen, T.-W. Ng, M.-F. Lo, C.-S. Lee **2018**, *30* 1800710.

[118] Y. Li, J. V. Milić, A. Ummadisingu, J.-Y. Seo, J.-H. Im, H.-S. Kim, Y. Liu, M. I. Dar, S. M. Zakeeruddin, P. Wang, A. Hagfeldt, M. Grätzel, *Nano Lett.* **2018**, *19*, 1 150.

[119] K. Lanty, Gaëtan ad Jemli, Y. Wei, J. Leymarie, J. Even, J.-S. Lauret, E. Deleporte, *J. Phys. Chem. Lett.* **2014**, *5* 3958.

[120] I. C. Smith, E. T. Hoke, D. Solis-Ibarra, M. D. McGehee, H. I. Karunadasa, *Angewandte Chemie International Edition* **2014**, *53*, 42 11232.

[121] L. Lanzetta, J. M. Marin-Beloqui, I. Sanchez-Molina, D. Ding, S. A. Haque, *ACS Energy Lett.* **2017**, *2* 1662.

[122] P. Cheng, T. Wu, J. Liu, W.-Q. Deng, K. Han, *J. Phys. Chem. Lett.* **2018**, *9* 2518.

[123] A. O. Polyakov, A. H. Arkenbout, J. Baas, G. R. Blake, A. Meetsma, A. Caretta, P. H. M. van Loosdrecht, T. T. M. Palstra, *Chem. Mater.* **2012**, *24* 133.

[124] D. Ma, Y. He, *J. Alloys Compound.* **2017**, 696 1213.

[125] M. E. Kamminga, H.-H. Fang, M. R. Filip, F. Giustino, J. Baas, G. R. Blake, M. A. Loi, T. T. M. Palstra, *Chem. Mater.* **2016**, *28*, 13 4554.

[126] Z. Li, N. Liu, K. Meng, Z. Liu, Y. Hu, Q. Xu, X. Wang, S. Li, L. Cheng, G. Chen, *Nano Lett.* **2019**, *19*, 8 5237.

[127] X.-H. Zhu, N. Mercier, A. Riou, P. Blanchard, P. Frère, *Chem. Commun.* **2002**, *2002*, 18 2160.

[128] G. Jia, Z.-J. Shi, Y.-D. Xia, Q. Wei, Y.-H. Chen, G.-C. Xing, W. Huang, *Opt. Express* **2018**, *26* A66.

[129] M. Daub, H. Hillebrecht, *Z. Kristallogr.* **2018**, *233*, 8 555.

[130] L. Wu, P. Lu, Y. Li, Y. Sun, J. Wong, K. Yang, *J. Mater. Chem. A* **2018**, *6* 24389.

[131] D. G. Billing, A. Lemmerer, *New J. Chem.* **2008**, *32* 1736.

[132] G. Tang, C. Yang, A. Stroppa, D. Fang, J. Hong, *J. Chem. Phys.* **2017**, *146* 224702.

[133] T. Hu, M. D. Smith, E. R. Dohner, M.-J. Sher, X. Wu, M. T. Trinh, A. Fisher, J. Corbett, X.-Y. Zhu, H. I. Karunadasa, A. M. Lindenberg, *J. Phys. Chem. Lett.* **2016**, *7* 2258.

[134] Y. Zhang, P. Wang, M.-C. Tang, D. Barrit, W. Ke, J. Liu, T. Luo, Y. Liu, T. Niu, D.-M. Smilgies, Z. Yang, Z. Liu, S. Jin, M. G. Kanatzidis, A. Amassian, S. F. Liu, K. Zhao, *J. Am. Chem. Soc.* **2019**, *141*, 6 2684.

[135] J.-P. Li, L.-H. Li, L.-M. Wu, L. Chen, *Inorg. Chem.* **2009**, *48* 1260.

[136] J.-H. Im, H.-S. Kim, N.-G. Park, *APL Mater.* **2014**, *2* 081510.

[137] J. van Embden, A. S. R. Chesman, J. J. Jasieniak, *Chem. Mater.* **2015**, *27* 2246.

[138] O. Yaffe, A. Chernikov, Z. M. Norman, Y. Zhong, A. Velauthapillai, A. van der Zande, J. S. Owen, T. F. Heinz, *Phys. Rev. B* **2015**, *92* 045414.

- [139] Z. Guo, X. Wu, T. Zhu, X. Zhu, L. Huang, *ACS Nano* **2016**, *10* 9992.
- [140] Y. Lin, Y. Bai, Y. Fang, Z. Chen, S. Yang, X. Zheng, S. Tang, Y. Liu, J. Zhao, J. Huang, *J. Phys. Chem. Lett.* **2018**, *9* 654.
- [141] G. Lanty, A. Bréhier, R. Parashkov, J. S. Lauret, E. Deleporte, *New J. Phys.* **2008**, *10* 065007.
- [142] Z. Xiao, W. Meng, B. Saparov, H.-S. Duan, C. Wang, C. Feng, W.-Q. Liao, W. Ke, D. Zhao, J. Wang, D. B. Mitzi, Y. Yan, *J. Phys. Chem. Lett.* **2016**, *7* 1213.
- [143] Y. Sun, L. Zhang, N. Wang, S. Zhang, Y. Cao, Y. Miao, M. Xu, H. Zhang, H. Li, C. Yi, J. Wang, W. Huang, *npj Flexible Electronics* **2018**, *2* 12.
- [144] S. Zhang, P. Audebert, Y. Wei, A. Al Choueiry, G. Lanty, A. Bréhier, L. Galmiche, G. Clavier, C. Boissière, J.-S. Lauret, E. Deleporte, *Materials* **2010**, *3* 3385.
- [145] S.-Q. Luo, J.-F. Wang, B. Yang, Y.-B. Yuan, *Front. Phys.* **2019**, *14* 53401.
- [146] J. Chen, Y. Wang, L. Gan, Y. He, H. Li, T. Zhai, *Angew. Chem. Int. Ed.* **2017**, *56* 14893.
- [147] X. Wu, M. T. Trinh, D. Niesner, H. Zhu, Z. Norman, J. S. Owen, O. Yaffe, B. J. Kudisch, X.-Y. Zhu, *J. Am. Chem. Soc.* **2015**, *137* 2089.
- [148] K. Abdel-Baki, F. Boitier, H. Diab, G. Lanty, K. Jemli, F. Lédée, D. Garrot, E. Deleporte, J. S. Lauret, *J. Appl. Phys.* **2016**, *119* 064301.
- [149] D. Cortecchia, K. C. Lew, J.-K. So, A. Bruno, C. Soci, *Chem. Mater.* **2017**, *29* 10088.
- [150] J. Chen, L. Gan, F. Zhuge, H. Li, J. Song, H. Zeng, T. Zhai, *Angew. Chem. Int. Ed.* **2017**, *56* 2390.

[151] R. Younts, H.-S. Duan, B. Gautam, B. Saparov, J. Liu, C. Mongin, F. N. Castellano, D. B. Mitzi, K. Gundogdu, *Adv. Mater.* **2016**, *29* 1604278.

[152] R. Hamaguchi, M. Yoshizawa-Fujita, T. Miyasaka, H. Kunugita, K. Ema, Y. Takeoka, M. Rikukawa, *Chem. Commun.* **2017**, *53* 4366.

[153] T. M. Koh, V. Shanmugam, J. Schlipf, L. Oesinghaus, P. Müller-Buschbaum, N. Ramakrishnan, V. Swamy, N. Mathews, P. P. Boix, S. G. Mhaisalkar, *Adv. Mater.* **2016**, *28* 3653.

[154] N. R. Venkatesan, J. G. Labram, M. L. Chabinye, *ACS Energy Lett.* **2018**, *3* 380.

[155] C. M. Raghavan, T.-P. Chen, S.-S. Li, W.-L. Chen, C.-Y. Lo, Y.-M. Liao, G. Haider, C.-C. Lin, C.-C. Chen, R. Sankar, Y.-M. Chang, F.-C. Chou, C.-W. Chen, *Nano Lett.* **2018**, *18* 3221.

[156] M. Xiao, F. Huang, W. Huang, Y. Dkhissi, Y. Zhu, J. Etheridge, A. Gray-Weale, U. Bach, Y.-B. Cheng, L. Spiccia, *Angew. Chem. Int. Ed.* **2014**, *53* 9898.

[157] N. Zhou, Y. Shen, L. Li, S. Tan, N. Liu, G. Zheng, Q. Chen, H. Zhou, *J. Am. Chem. Soc.* **2018**, *140* 459.

[158] E. Shi, Y. Gao, B. P. Finkenauer, Akriti, A. H. Coffey, L. Dou, *Chem. Soc. Rev.* **2018**, *47* 6046.

[159] J.-C. Blancon, H. Tsai, W. Nie, C. C. Stoumpos, L. Pedesseau, C. Katan, M. Kepenekian, C. M. M. Soe, K. Appavoo, M. Y. Sfeir, S. Tretiak, P. M. Ajayan, M. G. Kanatzidis, J. Even, J. J. Crochet, A. D. Mohite, *Science* **2017**, *355* 1288.

[160] W. Peng, J. Yin, K.-T. Ho, O. Ouellette, M. De Bastiani, B. Murali, O. El Tall, C. Shen, X. Miao, J. Pan, E. Alarousu, J.-H. He, B. S. Ooi, O. F. Mohammed, E. Sargent, O. M. Bakr, *Nano Lett.* **2017**, *17* 4759.

[161] D. Cortecchia, S. Neutzner, A. R. Srimath Kandada, E. Mosconi, D. Meggiolaro, F. De Angelis, C. Soci, A. Petrozza, *J. Am. Chem. Soc.* **2017**, *139* 39.

- [162] Q. Xu, B. Schmidt, S. Pradhan, M. Lipson, *Nature* **2005**, *435*, 7040 325.
- [163] S. M. Sze, K. K. Ng, *Physics of semiconductor devices*, John Wiley & sons, **2006**.
- [164] T. Umebayashi, K. Asai, T. Kondo, A. Nakao, *Phys. Rev. B* **2003**, *67* 155405.
- [165] B. Saporov, F. Hong, J.-P. Sun, H.-S. Duan, W. Meng, S. Cameron, I. G. Hill, Y. Yan, D. B. Mitzi, *Chem. Mater.* **2015**, *27* 5622.
- [166] S. Fujita, *Jpn. J. Appl. Phys* **2015**, *54*, 3 030101.
- [167] H. Tan, F. Che, M. Wei, Y. Zhao, M. I. Saidaminov, P. Todorović, D. Broberg, G. Walters, F. Tan, T. Zhuang, et al., *Nat. Commun.* **2018**, *9*, 1 1.
- [168] C. Bernal, K. Yang, *J. Phys. Chem. C* **2014**, *118* 24383.
- [169] A. Fraccarollo, L. Canti, L. Marchese, M. Cossi, *J. Chem. Phys.* **2017**, *146* 234703.
- [170] J. I. Pankove, *Optical Processes in Semiconductors*, Dover publications (New York), **1975**.
- [171] T. Wang, B. Daiber, J. M. Frost, S. A. Mann, E. C. Garnett, A. Walsh, B. Ehrler, *Energy Environ. Sci.* **2017**, *10* 509.
- [172] M. A. Green, A. Ho-Baillie, H. J. Snaith **2014**, *8* 506.
- [173] J. Tauc, R. Grigorovici, A. Vancu, *Phys. Stat. Solidi (B)* **1966**, *15* 627.
- [174] B. Ohtani, *Phys. Chem. Chem. Phys.* **2014**, *16* 1788.

[175] H. Störmer, R. Dingle, A. Gossard, W. Wiegmann, M. Sturge, *Solid State Commun.* **1979**, 29 705.

[176] W. Liu, J. Xing, J. Zhao, X. Wen, K. Wang, P. Lu, Q. Xiong, *Adv. Opt. Mater.* **2017**, 5 1601045.

[177] Z.-K. Tan, R. S. Moghaddam, M. L. Lai, P. Docampo, R. Higler, F. Deschler, M. Price, A. Sadhanala, L. M. Pazos, D. Credgington, F. Hanusch, T. Bein, H. J. Snaith, R. H. Friend, *Nat. Nanotechnol.* **2014**, 9 687.

[178] Y.-H. Kim, C. Himchan, J. H. Heo, T.-S. Kim, u. Myoung NoSo, C.-L. Lee, H. Im Sang, T.-W. Lee, *Adv. Mater.* **2014**, 27 1248.

[179] R. Meerheim, S. Scholz, S. Olthof, G. Schwartz, S. Reineke, K. Walzer, K. Leo, *J. Appl. Phys.* **2008**, 104 014510.

[180] C. Adachi, M. A. Baldo, M. E. Thompson, S. R. Forrest, *J. Appl. Phys.* **2001**, 90 5048.

[181] H. Aziz, Z. D. Popovic, *Chem. Mater.* **2004**, 16 4522.

[182] J. S. Ross, P. Klement, A. M. Jones, N. J. Ghimire, J. Yan, D. G. Mandrus, T. Taniguchi, K. Watanabe, K. Kitamura, W. Yao, D. H. Cobden, X. Xu, *Nat. Nanotechnol.* **2014**, 9 268.

[183] J. Ross, S. Wu, H. Yu, N. Ghimire, A. Jones, G. Aivazian, J.-Q. Yan, D. G. Mandrus, X. di, W. Yao, X. Xu, *Nat. Commun.* **2013**, 4 1474.

[184] S. Wu, S. Buckley, A. Jones, J. Ross, N. Ghimire, J.-Q. Yan, D. G. Mandrus, W. Yao, F. Hatami, J. Vuckovic, A. Majumdar, X. Xu, *2D Mater.* **2013**, 1 011001.

[185] D. Saporì, M. Kepenekian, L. Pedesseau, C. Katan, J. Even, *Nanoscale* **2016**, 8 6369.

[186] Y. Sun, N. C. Giebink, H. Kanno, B. Ma, M. E. Thompson, S. R. Forrest, *Nature* **2006**, 440 908.

[187] B. W. D'Andrade, S. R. Forrest, *Adv. Mater.* **2004**, 16 1585.

[188] Y. Shiraishi, H. Hara, T. Hirai, I. Komasa, *Ind. Eng. Chem. Res.* **1999**, 38 1589.

[189] Y. Liu, J. Zhao, *Chem. Commun.* **2012**, 48 3751.

[190] Q. Liu, B. Yin, T. Yang, Y. Yang, Z. Shen, P. Yao, F. Li, *J. Am. Chem. Soc.* **2013**, 135 5029.

[191] A. D. Vos, *J. Phys. D: Appl. Phys.* **1980**, 13 839.

[192] Z. M. Beiley, M. D. McGehee, *Energy Environ. Sci.* **2012**, 5 9173.

[193] C. M. Mauck, W. A. Tisdale, *Trends in Chemistry* **2019**, 1 380.

[194] Y. Liu, H. Xiao, W. A. Goddard, *Nano Lett.* **2016**, 16 3335.

[195] P. Koenraad, M. Flatté, *Nat. Mater.* **2011**, 10 91.

[196] J. M. Ball, A. Petrozza, *Nature Energy* **2016**, 1 16149.

[197] H. Jin, E. Debroye, M. Keshavarz, I. G. Scheblykin, M. B. J. Roeffaers, J. Hofkens, J. A. Steele, *Mater. Horiz.* **2020**, 7, 2 397.

[198] T. Leijtens, S. D. Stranks, G. E. Eperon, R. Lindblad, E. M. J. Johansson, I. J. McPherson, H. Rensmo, J. M. Ball, M. M. Lee, H. J. Snaith, *ACS Nano* **2014**, 8 7147.

[199] L. Wang, C. McCleese, A. Kovalsky, Y. Zhao, C. Burda, *J. Am. Chem. Soc.* **2014**, 136 12205.

- [200] W.-J. Yin, T. Shi, Y. Yan, *Adv. Mater.* **2014**, *26* 4653.
- [201] W.-J. Yin, T. Shi, Y. Yan, *Appl. Phys. Lett.* **2014**, *104* 063903.
- [202] M. M. Vopson, *Crit. Rev. Solid State Mater. Sci.* **2015**, *40*, 4 223.
- [203] M. Gajek, M. Bibes, A. Barthélémy, K. Bouzehouane, S. Fusil, M. Varela, J. Fontcuberta, A. Fert, *Phys. Rev. B* **2005**, *72*, 2 020406.
- [204] J. Ryu, A. V. Carazo, K. Uchino, H.-E. Kim, *Japanese Journal of Applied Physics* **2001**, *40*, 8R 4948.
- [205] M. M. Vopson, *J. Phys. D: Appl. Phys.* **2013**, *46*, 34 345304.
- [206] L. Li, X. Liu, Y. Li, Z. Xu, Z. Wu, S. Han, K. Tao, M. Hong, J. Luo, Z. Sun, *J. Am. Chem. Soc.* **2019**, *141* 2623.
- [207] R. D. Willett, *Acta Cryst. C* **1990**, *46* 565.
- [208] W. E. Estes, D. B. Losee, W. E. Hatfield, *J. Chem. Phys.* **1980**, *72* 630.
- [209] A. H. Arkenbout, T. Uemura, J. Takeya, T. T. M. Palstra, *Appl. Phys. Lett.* **2009**, *95* 173104.
- [210] L. N. Quan, M. Yuan, R. Comin, O. Voznyy, E. M. Beauregard, S. Hoogland, A. Buin, A. R. Kirmani, K. Zhao, A. Amassian, D. H. Kim, E. H. Sargent, *J. Am. Chem. Soc.* **2016**, *138* 2649.
- [211] D. Lin, T. Zhang, J. Wang, M. Long, F. Xie, J. Chen, B. Wu, T. Shi, K. Yan, W. Xie, P. Liu, J. Xu, *Nano Energy* **2019**, *59* 619.
- [212] A. A. Sutanto, N. Drigo, V. I. E. Queloz, I. Garcia-Benito, A. R. Kirmani, L. J. Richter, P. A. Schouwink, K. T. Cho, S. Paek, M. K. Nazeeruddin, G. Grancini, *Journal of*

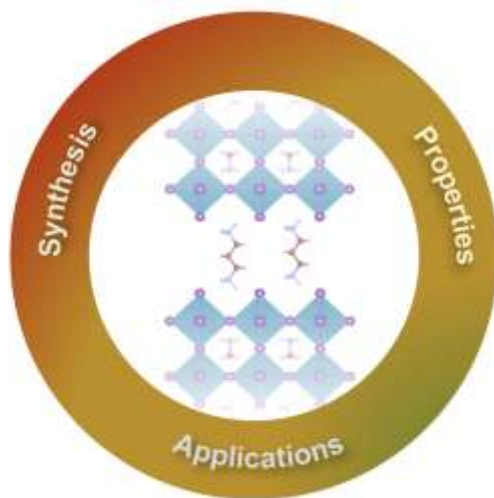
- [213] Y. Liu, S. Akin, L. Pan, R. Uchida, N. Arora, J. V. Milić, A. Hinderhofer, F. Schreiber, A. R. Uhl, S. M. Zakeeruddin, A. Hagfeldt, M. I. Dar, M. Grätzel, *Sci. Adv.* **2019**, *5*, 6 eaaw2543.
- [214] A. Krishna, S. Gottis, M. K. Nazeeruddin, F. Sauvage, *Adv. Fun. Mater.* **2019**, *29* 1806482.
- [215] F. Zhang, D. H. Kim, K. Zhu, *Curr. Opin. Electrochem.* **2018**, *11* 105.
- [216] C. Huo, B. Cai, Z. Yuan, B. Ma, H. Zeng, *Small Methods* **2017**, *1* 1600018.
- [217] E. F. Schubert, J. Cho, J. K. Kim, *Light-Emitting Diodes*, John Wiley & Sons, Inc, **2015**.
- [218] Z. Tan, Y. Wu, H. Hong, J. Yin, J. Zhang, L. Lin, M. Wang, X. Sun, L. Sun, Y. Huang, K. Liu, Z. Liu, H. Peng, *J. Am. Chem. Soc.* **2016**, *138* 16612.
- [219] L. Niu, Q. Zeng, J. Shi, C. Cong, C. Wu, F. Liu, J. Zhou, W. Fu, Q. Fu, C. Jin, T. Yu, X. Liu, Z. Liu **2016**, *26*, 29 5263.
- [220] S. Han, Y. Yao, X. Liu, B. Li, C. Ji, Z. Sun, M. Hong, J. Luo, *Small* **2019**, *15*, 39 1901194.
- [221] Y. Li, K. Yang, *Energy Environ. Sci.* **2019**, *12* 2233.
- [222] Y. Li, D. Maldonado-Lopez, V. Ros Vargas, J. Zhang, K. Yang, *J. Chem. Phys.* **2020**, *152* 084106.
- [223] T. Nakajima, K. Sawada, *J. Phys. Chem. Lett.* **2017**, *8* 4826.
- [224] S. Lu, Q. Zhou, Y. Ouyang, Y. Guo, Q. Li, J. Wang, *Nat. Commun.* **2018**, *9* 3405.

- [225] Y. Chen, Y. Lei, Y. Li, Y. Yu, J. Cai, M.-H. Chiu, R. Rao, Y. Gu, C. Wang, W. Choi, H. Hu, C. Wang, Y. Li, J. Song, J. Zhang, B. Qi, M. Lin, Z. Zhang, A. E. Islam, B. Maruyama, S. Dayeh, L.-J. Li, K. Yang, Y.-H. Lo, S. Xu, *Nature* **2020**, 577 209.
- [226] S. Nazir, M. Behtash, K. Yang, *Appl. Phys. Lett.* **2014**, 105 141602.
- [227] S. Nazir, K. Yang, *ACS Appl. Mater. Interfaces* **2014**, 6 22351.
- [228] S. Nazir, S. Jiang, J. Cheng, K. Yang, *Appl. Phys. Lett.* **2019**, 114 072407.
- [229] S. Jiang, S. Nazir, K. Yang, *Phys. Rev. B* **2020**, 101 134405.
- [230] Y. Wang, W. Tang, J. Cheng, M. Behtash, K. Yang, *ACS Appl. Mater. Interfaces* **2016**, 8 13659.
- [231] S. Nazir, J. Cheng, K. Yang, *ACS Appl. Mater. Interfaces* **2016**, 8 390.
- [232] J. V. Passarelli, D. J. Fairfield, N. A. Sather, M. P. Hendricks, H. Sai, C. L. Stern, S. I. Stupp, *J. Am. Chem. Soc.* **2018**, 140, 23 7313.
- [233] Y. Gao, E. Shi, S. Deng, S. B. Shiring, J. M. Snaider, C. Liang, B. Yuan, R. Song, S. M. Janke, A. Liebman-Peláez, et al., *Nat. Chem.* **2019**, 11, 12 1151.
- [234] Y. Gao, Z. Wei, P. Yoo, E. Shi, M. Zeller, C. Zhu, P. Liao, L. Dou, *J. Am. Chem. Soc.* **2019**, 141, 39 15577.
- [235] J. Ma, C. Fang, C. Chen, L. Jin, J. Wang, S. Wang, J. Tang, D. Li, *ACS Nano* **2019**, 13, 3 3659.
- [236] J. Ahn, S. Ma, J.-Y. Kim, J. Kyhm, W. Yang, J. A. Lim, N. A. Kotov, J. Moon, *J. Am. Chem. Soc.* **2020**, 142, 9 4206.
- [237] A. Vassilakopoulou, D. Papadatos, I. Koutselas, *Appl. Sur. Sci.* **2017**, 400 434.

[238] H. Lu, J. Wang, C. Xiao, X. Pan, X. Chen, R. Brunecky, J. J. Berry, K. Zhu, M. C. Beard, Z. V. Vardeny, *Sci. Adv.* **2019**, 5 eaay0571.

Accepted Article

Table of Contents



Recent research progress of the two-dimensional hybrid halide perovskites including their synthesis approaches, structural characterization, optoelectronic and multiferroic properties, defect states, moisture stability, and related devices and applications are reviewed, along with their computational and theoretical studies.

Author Biographies for Solar RRL

Joseph Wong received his B.S. in Chemical Engineering in 2018 and M.S. in Nanoengineering in 2019 from the Department of NanoEngineering at the University of California San Diego. He was an undergraduate/master's student under the supervision of Prof. Kesong Yang between 2016-2019. Currently, he is a Quality Engineer at Boeing Commercial Airlines for the 777 Program. His research interests focus on the application of computational techniques for the analysis of hybrid perovskites for stable, high-efficiency solar cells and magnetic Heusler alloys for memory storage devices.



Kesong Yang is an Associate Professor in the Department of NanoEngineering at University of California San Diego (UC San Diego). He received his Ph.D. degree in Atomic and Molecular Physics from Shandong University, China, in 2010, and worked as a visiting Ph.D. student at National University of Singapore in 2009. Before he joined UC San Diego in 2013, he worked in the Duke University as a Postdoctoral Researcher. His research interests include computational studies of functional materials and algorithm development for high-throughput materials design. His current research focuses on the high-throughput design of perovskite-based functional materials and materials interfaces.



Accepted